UNIVERSITÉ DU QUÉBEC À MONTRÉAL

NUMERICAL MODELLING OF LATERAL VISCOSITY VARIATIONS IN THE EARTH'S MANTLE

THESIS SUBMITTED AS A PARTIAL REQUIREMENT
FOR THE DEGREE OF MASTER OF SCIENCE
IN EARTH SCIENCES

BY

MARIE NICOLE THOMAS

DECEMBER 2017

UNIVERSITÉ DU QUÉBEC À MONTRÉAL

LA MODÉLISATION NUMÉRIQUE DES VARIATIONS LATÉRALES DE VISCOSITÉ DANS LE MANTEAU TERRESTRE

MÉMOIRE PRÉSENTÉ
COMME EXIGENCE PARTIELLE
DE LA MAÎTRISE EN SCIENCES DE LA TERRE

PAR
MARIE NICOLE THOMAS

DÉCEMBRE 2017

ACKNOWLEDGEMENTS

This work would not have been possible without the teachings, patience, and funding of my supervisor Alessandro Forte; nor without continual assistance and advice from Petar Glišović, my windowless laboratory companion. I'm also very grateful to Fiona Darbyshire for her excellent lectures, kind words, and generous support; and to Olivia Jensen, whose gracious assistance helped me to avoid the "leaky pipeline" of female physicists.

Many others have helped me complete this work; in particular, Utkarsh Ayachit provided valuable support through the ParaView mailing list, and Jacqueline Austermann kindly shared her script for visualising dynamic topography output from ASPECT.

Computations for this thesis were made on the supercomputer Briarée from the Université de Montréal, managed by Calcul Québec and Compute Canada and funded by the Canada Foundation for Innovation (CFI), the ministère de l'Économie, de la science et de l'innovation du Québec (MESI) and the Fonds de recherche du Québec - Nature et technologies (FRQ-NT). Additional simulations were run on the HiPerGator 2.0 supercomputer at the University of Florida.

CONTENTS

LIST OF TABLES

LIST OF FIGURES

LIST OF ABBREVIATIONS

AMR	adaptive mesh refinement
ASPECT	Advanced Solver for Problems in Earth's ConvecTion
CitComS	California Institute of Technology Convection in the Mantle - Spherical
CMB	core–mantle boundary
DOF	degrees of freedom
EPR	East Pacific Rise
FEM	finite element method
GIA	glacial isostatic adjustment
GPS	Global Positioning System
HPG2	HiPerGator 2.0
LVV	lateral viscosity variations
PREM	Preliminary Reference Earth Model
RVV	radial viscosity variations
WPB	weak plate boundaries
VTU	Visualization Toolkit Unstructured

RÉSUMÉ

Cette étude modélise l'écoulement instantané du manteau terrestre en utilisant le code source ouvert ASPECT. Elle examine surtout l'impact des variations latérales de viscosité sur l'écoulement mantellique et sur la topographie dynamique de la surface.

On utilise le profil de viscosité 'V2' de Mitrovica et Forte (2004), qui ne varie qu'en fonction de la profondeur. La composante latérale de la viscosité est calculée en supposant qu'elle dépend de la température selon une loi de type Arrhenius. Les variations de température viennent du modèle de tomographie sismique GyPSuM, qui intègre des données géodynamiques et des résultats d'expériences en physique des minéraux (Simmons *et al.*, 2010). Les comparaisons entre des résultats obtenus par GyPSuM et par S40RTS, autre modèle de tomographie sismique de Ritsema *et al.* (2011), confirment que des vitesses des ondes de cisaillement ne suffisent pas pour résoudre la structure complexe du manteau terrestre.

De façon général, on trouve que les variations latérales de viscosité augmentent la vigueur de l'écoulement du manteau et atténuent la topographie dynamique de la surface. On cherche à varier l'amplitude des variations latérales de viscosité, mais la résolution numérique de ASPECT a du mal à converger même pour les variations modeste. On abordera des solutions et des orientations possibles pour des travaux futurs.

Mots clés: convection mantellique, rhéologie du manteau, viscosité, topographie dynamique, tomographie sismique

ABSTRACT

The open-source code ASPECT is used to model the impact of lateral viscosity variations on instantaneous mantle flow and dynamic topography.

The initial viscosity follows the geodynamically inferred 'V2' profile of Mitrovica and Forte (2004) which varies with depth alone. The lateral component of the viscosity is computed assuming an Arrhenius-type temperature dependence, with the perturbed temperature field given by the seismic tomography model GyPSuM, which uniquely incorporates data from geodynamic observations and mineral physics experiments (Simmons *et al.*, 2010). Comparisons between GyPSuM and the S40RTS seismic tomography model of Ritsema *et al.* (2011) confirms earlier findings that shear-wave velocities alone are not sufficient to characterise the complex, three-dimensional heterogeneities of the Earth's mantle.

In general, lateral viscosity variations are found to increase the vigour of mantle flow and to moderate the amplitude of dynamic topography. Different amplitudes are also investigated, but the ASPECT numerical solver demonstrates convergence problems beyond modest lateral viscosity contrasts. Possible solutions and directions for future work are discussed.

Keywords: mantle convection, mantle rheology, viscosity, dynamic topography, seismic tomography

INTRODUCTION

Viscosity is a key parameter in the study of thermal convection in the Earth's mantle. The present study seeks to investigate mantle viscosity using the tools of computational geodynamics, and specifically will examine the significance of lateral variations of viscosity in global simulations of mantle convection. The first chapter will develop a theoretical foundation to guide the chapters that follow, underlining the complex rheology of the mantle and introducing the mathematical equations that govern thermal convection.

To provide more specific context for this work, the second chapter will review past literature on the subject of lateral viscosity variations (LVV). We can infer from seismic data, convection-related observables, and mineral physics experiments that mantle rheology varies significantly not only with depth, but also laterally (e.g., Forte *et al.*, 2010). Large LVV spanning three or more orders of magnitude are necessary to account for stiff cratons and weak plate boundary zones in the lithosphere (e.g., Ghosh *et al.*, 2010). Mantle flow models that incorporate LVV can also predict seismic anisotropy (e.g., Becker *et al.*, 2008). It can be numerically challenging to implement LVV in the whole mantle, but comprehensive models should incorporate LVV on principle, as realistic mantle flow cannot be generated in their absence (e.g., Rogozhina, 2008; Forte *et al.*, 2015).

The third chapter will present an overview of computational geodynamics, focusing mainly on the finite element method employed by ASPECT, or *Advanced Solver for Problems in Earth's ConvecTion* (Kronbichler *et al.*, 2012), the open-source mantle convection code used for this study. The methods and results of the numerical model will be presented in the fourth chapter, with an emphasis on how mantle flow and dynamic surface topography change when LVV are taken into account. Finally, the conclusion will review important highlights from this work and propose directions for future research.

CHAPTER I

AN OVERVIEW OF MANTLE DYNAMICS

1.1 Historical background

The puzzle-piece match between West Africa and the east coast of South America propelled a few intrepid scientists towards the theory of continental drift in the early 20th century. Chief among them were Frank Bursley Taylor and Alfred Wegener, the latter of whom published an entire book on the subject in 1915. However, Wegener's ideas were widely panned by the scientific community. Critically, he had failed to provide a plausible mechanism that could drive these proposed surface movements (Schubert *et al.*, 2004). Continental drift remained a fringe theory until it was revived by a growing body of evidence, including the discovery of a rift on the Mid-Atlantic Ridge by Marie Tharp in the 1950s (Barton, 2002).

Tharp's collaborator Bruce Heezen inferred that the Mid-Atlantic Ridge was an extensional structure and concluded that the Earth must be gaining volume over time (Davies, 2000). Dietz (1961) and Hess (1962) generally accepted the first premise but rejected the notion of an expanding Earth. Both proposed independently that new crustal material is formed at spreading ocean ridges, and that deep ocean trenches are areas of crustal convergence where the Earth's surface area may be lost, a process later identified as subduction. Direct evidence of seafloor spreading was identified by Vine and Matthews (1963) and Morley and Larochelle (1964), who correctly interpreted the magnetic stripes observed running parallel to ocean ridges as reversals in the polarity of the Earth's magnetic field over time. Emergent oceanic crust acquires *thermoremanent magnetisation* as it cools in the presence of the Earth's magnetic field and can preserve a record of the magnetic field direction while moving away from the spreading ridge over time. Continental drift, seafloor spreading, and subduction were combined into a unified model of global plate tectonics by the late 1960s, with significant contributions from Tuzo Wilson (Schubert *et al.*, 2004). However, plate tectonics is a kinematic model and cannot account for the driving force that was missing from Wegener's description of continental drift.

Dietz and Hess had both proposed large-scale thermal convection cells in the mantle as providing the motive force behind seafloor spreading. Tozer (1965) argued that mantle convection is inevitable due to the strong temperature dependence of silicate rheology, and Turcotte and Oxburgh (1967) related plate tectonics and mantle convection through a simple convection model in which the lithosphere was conceived as an upper thermal boundary layer that could travel along the top of a convection cell before descending. Mantle convection has since been recognised as the driving mechanism behind the Earth's horizontal surface motions: cold material subducts and sinks, while hot material rises from the mantle to form fresh crust on the ocean floor. In Wegener's time, the mantle was still considered too rigid to permit thermal convection, but shortly after the Mid-Atlantic Ridge was discovered, spreading of the ocean floor was also confirmed. The continental puzzle pieces had indeed been driven apart.

Though impossible to observe directly, the dynamic mantle expresses itself clearly through surface processes and other measurable phenomena, such as the geoid—an equipotential surface that undulates according to gravity perturbations across the globe, revealing information about the heterogeneous structure and composition of the solid Earth below. Glacial isostatic adjustment, or the ongoing relaxation of surface bulges and depressions formed under the weight of massive ice sheets during the Last Glacial

Maximum, provides further evidence of a non-rigid mantle.

The mantle is not a rigid body, but neither can it be described as having a true elastic response to applied stresses. Instead, the deformation of mantle rocks can be characterised as mainly elastic or viscous depending on the time scale of the applied stress: a property termed *viscoelasticity*. The following sections will explore this dual nature more thoroughly and present the physical and rheological laws that govern the long-term dynamics of the Earth's mantle.

1.2 Mantle rheology

Rheology describes the flow and deformation of a viscous material. The mantle is *viscoelastic*, responding in an elastic or viscous manner depending on the time scale of an applied stress. For deformations occurring on short to intermediate time scales, anelastic (nearly elastic) processes dominate. This applies to seismic waves, free oscillations of the Earth, body tides, and the Chandler wobble. On time scales in excess of a few hundred years, the solid Earth exhibits fluid behaviour, giving rise to mantle convection and related geodynamic processes.

Viscoelastic materials are sometimes described as *Maxwell fluids*, and the characteristic time that separates anelastic deformation and viscous creep behaviour is referred to as the *Maxwell time*, given by the following:

$$T_m = \frac{\eta}{\mu} \tag{1.1}$$

where η is the long-term viscosity and μ is the elastic modulus of rigidity. Average values for the Earth's mantle are $\eta = 10^{21}\ \mathrm{Pa \cdot s}$ and $\mu = 100\ \mathrm{GPa}$, which together give $T_m \approx 300\ \mathrm{years}$. The transition time range is poorly understood, but ample geophysical evidence exists to support the short-term anelastic and long-term viscous comportment of mantle rocks (Forte, 2014).

1.2.1 Geophysical evidence for short-term elastic behaviour

Seismic waves provide a clear illustration of the solid Earth as an anelastic body. Body waves propagate through the mantle with only a small amount of energy loss, indicating travel through an imperfect elastic medium rather than a fluid. In particular, shear waves would not be able to propagate through the mantle at all if it did not have sufficient shear strength. Small energy attenuations, in which seismic waves lose vibrational energy as heat, nonetheless reveal something of the viscous character of the Earth (Karato, 2003). This energy dissipation may be characterised by a "transient" viscosity (Anderson and Minster, 1979). Body waves have very short periods, typically ranging from milliseconds to about a minute.

Earthquakes can also trigger the whole planet to vibrate like a struck bell, exciting the *free oscilllations* of the Earth. Just as a vibrating string can be described in terms of its characteristic normal modes, the displacement of the solid Earth can be represented as the sum of one or more natural modes of vibration. *Spheroidal modes* describe radial displacements inwards or outwards, while *torsional modes* represent displacements parallel to the surface. Different free-oscillation modes of the Earth have been measured with periods as short as just a few minutes and up to nearly one hour (Benioff *et al.*, 1961). These measurements correspond to elasto-gravitational deformation that would not be physically possible if the solid Earth behaved like a fluid on this time scale.

On a slightly longer time scale, the solid Earth experiences *body tides* under the gravitational influence of the Sun and Moon. This deformation would not occur if the Earth were completely rigid, and it would be much more pronounced if the solid Earth were fluid. Body tides are also an elasto-gravitational deformation. Although numerous different periods exist, the principal tides are semi-diurnal, with periods of approximately

12 hours; and diurnal, with periods of approximately 24 hours (Melchior, 1966).

The *Chandler wobble*, a free nutation of the Earth, provides further support of the mantle's anelastic behaviour on an intermediate time scale. The Chandler wobble is a principal component of polar wander and results from an uneven distribution of mass that displaces Earth's instantaneous rotational axis (Lowrie, 2007). The calculated period of this nutation is only about 305 days for an unyielding rigid-body Earth, while the observed Chandler wobble has $T \sim 435$ days. However, taking anelastic deformation into consideration together with surface oceans and a fluid outer core, calculated values are brought into close agreement with the observed period (Anderson and Minster, 1979).

1.2.2 Geophysical evidence for long-term viscous behaviour

When stresses are applied over geological time scales, the mantle appears to behave in a purely viscous manner. Some examples are continental drift driven by mantle convection, and postglacial rebound in formerly glaciated regions. Other supporting evidence includes crustal isostasy and the agreement between the hydrostatic ellipticity of a rotating liquid and the flattening of the rotating Earth. This behaviour is characterised by a long-term or "steady-state" viscosity.

On millennial time scales, we can observe *glacial isostatic adjustment* (GIA): ongoing uplift and subsidence of the Earth's surface in response to the retreat and eventual disappearance of massive ice sheets since the end of the Last Glacial Maximum. Both the Laurentide and Fennoscandian ice sheets totally melted between 6,000 and 8,000 years ago and are a rich source of GIA data. In 1935, Norman Haskell was the first to estimate average mantle viscosity based on his analysis of Fennoscandian uplift. His estimate of about 10^{21} $\mathrm{Pa \cdot s}$ has endured, even being reproduced through joint inversions of Laurentide uplift data and other geophysical constraints (Mitrovica and Forte, 2004). This behaviour should not be confused with elastic deformation, which is completely recoverable. Here, when the glacial load is removed, buoyancy forces return the surface to equilibrium, but any deformation incurred by steady-state creep is permanent and can never be "reversed" in the thermodynamic sense (Van der Wal, 2009).

Thermal convection in the Earth's mantle occurs on even longer time scales, ranging from millions to hundreds of millions of years, and gives rise to the horizontal displacement of the Earth's tectonic plates and the associated phenomenon of continental drift. These surface motions have traditionally been inferred from paleomagnetic data, but GPS satellites can now provide direct measurements of plate velocities as well. Estimates of surface plate velocities from geologic and geodetic data sets are remarkably similar (Forte, 2014).

Gravity measurements have led to a few different results which further suggest a viscous mantle. By the 17th century, pendulums were being used to measure gravity anomalies across the world, leading scientists to believe that the Earth was not a perfect sphere, but an ellipsoid. Isaac Newton postulated in his *Principia Mathematica* that the Earth was an oblate spheroid, or flattened rather than football-shaped. One of his devotees, Alexis-Claude Clairaut, partook in an expedition to Lapland and developed his now-famous theorem to prove Newton's theory. Clairaut determined that, for a rotating fluid at equilibrium, the hydrostatic flattening is proportional to the square of the diurnal rotation rate. The present-day ellipticity of the Earth is remarkably similar to Clairaut's predictions for a rotating fluid, providing further evidence of the mantle's long-term fluid character (Forte, 2014).

The concept of crustal buoyancy, or *isostasy*, arose from studies of the low gravitational signals associated with high topography. In 1855, John Henry Pratt conducted a gravitational survey of the Himalayas and confirmed earlier findings that a plumb-

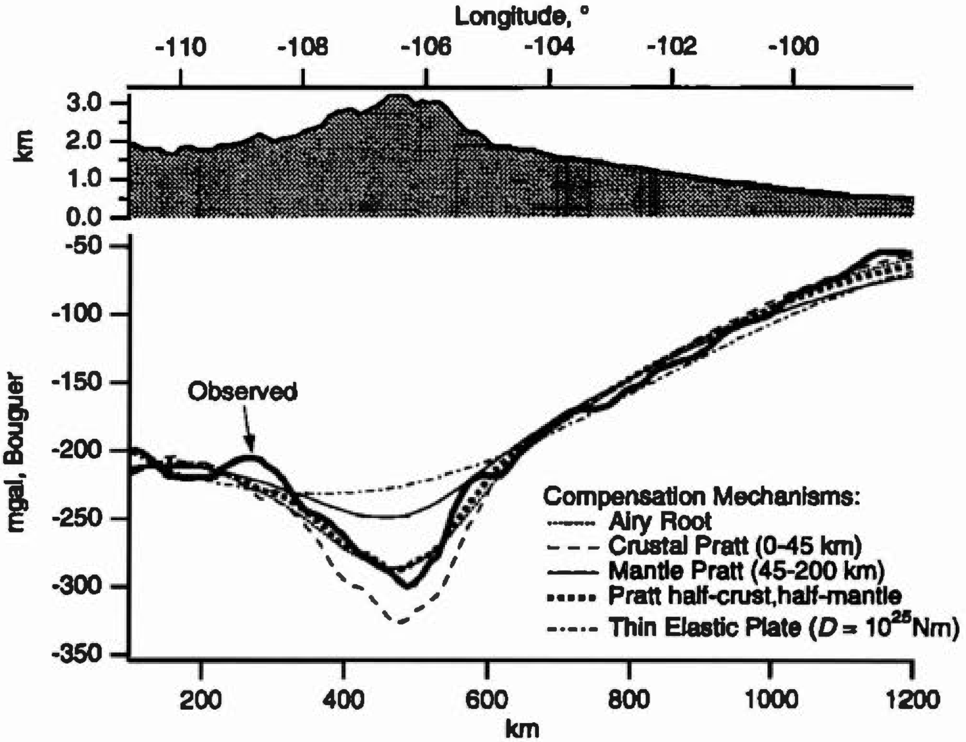

Figure 1.1: An illustration of isostatic compensation from Sheehan *et al.* (1995). The top section represents the positive topography of the Rocky Mountains, and the thick black line below represents the negative observed gravity anomaly. The various dotted lines represent the predicted gravity anomaly for different models of isostatic compensation.

bob deviated far less from vertical than expected, given estimates of the excess mass represented by the mountains (Lowrie, 2007). Continental crustal rocks are less dense than mantle rocks, but a mountain range sitting flat on a solid mantle would nonetheless create a positive gravity anomaly relative to lower-lying regions. However, low gravitational signals suggest that continents float on the mantle like an iceberg at sea, with deep roots displacing the surrounding mantle material. This displacement of denser material results in an overall deficit of mass and corresponding low-gravity anomaly, as shown in Figure 1.1. For a more nuanced discussion of isostasy, the reader is referred to Lowrie (2007).

Gravity anomalies associated with density heterogeneities in the deep mantle can similarly indicate long-term flow. For example, seismically fast regions below Pacific subduction zones produce negative gravity anomalies at the surface, despite being associated with accumulations of cold slabs. Slabs are compositionally similar to mantle rocks but are denser by virtue of being colder, permitting them to subduct (McKenzie *et al.*, 1974). Intuitively, the presence of positive density anomalies should produce positive gravity anomalies; however, in a convecting mantle, descending slabs are opposed by flow-induced dynamic topography which can result in overall negative gravity anomalies (Forte *et al.*, 2015).

1.2.3 Microphysical explanation

The previous examples clearly illustrate the mantle's ability to flow over geological time periods. Mineral physics provides an explanation for this long-term viscous behaviour: mantle rocks naturally contain atomic-scale defects in their crystalline structure, allowing dynamic processes like creep to occur under conditions of constant stress and elevated temperature. When these conditions are maintained for a sufficiently long time, the mantle achieves steady-state flow characterised by an effective viscosity η (Forte, 2014):

$$\eta = A d^m \tau^{-n} kT \exp\left(\frac{\Delta E + P\Delta V}{kT}\right) \tag{1.2}$$

where A is a dimensional constant, d is the effective grain size of mantle minerals, $\tau = \sqrt{\tau_{ij}\tau_{ij}}$ is the square root of the second invariant of the deviatoric stress field (see Section 1.3.1), k is Boltzmann's constant, T is the temperature, ΔE is the creep activation energy, P is the total pressure, and ΔV is the creep activation volume. The exponents m and n describe the sensitivity to grain size and stress, respectively.

Diffusion creep occurs at relatively low stress levels, small grain size, or both. This type of deformation results in diffusive mass transport between grain boundaries of mantle rocks, and the strain rate increases linearly with stress and depends significantly on grain size (Karato and Wu, 1993). In terms of Equation 1.2, the effective viscosity does not depend on stress ($n = 0$) while the grain-size sensitivity exponent m generally ranges from 2 to 3.

Dislocation creep occurs under conditions of high stress, large grain size, or both, and is also referred to as *power-law creep* due to the nonlinear relationship between stress and strain rate (Karato and Wu, 1993). Here, the effective viscosity depends on stress ($n \sim 3$) but not grain size ($m = 0$). This deformation results in the lattice-preferred orientation of minerals, and thus seismic anisotropy as well. This regime likely dominates in the shallow upper mantle.

Olivine and other mantle minerals have been studied extensively in laboratory deformation experiments in order to determine the rheology of the Earth's mantle. However, these results must be extrapolated to the irreproducible conditions of the mantle, where creep occurs on much longer time scales and at much lower stresses. The validity of such extrapolations is not clear (Karato, 2010). Olivine flow laws (e.g., Korenaga and Karato, 2008) are nevertheless used in many geodynamic models.

1.3 Mathematical background

The mantle can receive the same mathematical treatment as a fluid, owing to its liquid comportment over geological time. Different problems may call for different approaches, but the mantle as a whole is typically treated as a viscous Newtonian fluid in numerical simulations of thermal convection.

1.3.1 Governing equations

The fundamental equations of fluid dynamics are derived from the principles of conservation of mass, energy, and momentum (Landau and Lifshitz, 1987). The problem of mantle convection additionally requires an equation of state relating the density to temperature and pressure and a rheological description relating the stress and strain rate. The latter has already been described by Equation 1.2 in terms of the mantle's effective viscosity.

Considering an infinitesimal volume, conservation of mass implies that the rate of change of mass in the volume must be equal and opposite to the mass lost through flow:

$$\frac{\partial \rho}{\partial t} + \boldsymbol{\nabla} \cdot (\rho \mathbf{u}) = 0 \tag{1.3}$$

where ρ is the density and $\mathbf{u}$ is the flow velocity.

Next, conservation of energy implies that the rate of change of energy must be equal to the rate of heat production less the rates of heat loss through convection and conduction. This gives the temperature equation:

$$\rho c_p \frac{\partial T}{\partial t} = Q + \Phi + \alpha T \frac{dp}{dt} - \rho c_p \mathbf{u} \cdot \boldsymbol{\nabla} T - \boldsymbol{\nabla} \cdot (-k \boldsymbol{\nabla} T) \tag{1.4}$$

where c_p is the specific heat capacity, T is the temperature, Q is the rate of internal heat production, Φ represents frictional heat dissipation, $\alpha T \frac{dp}{dt}$ corresponds to adiabatic compression of material with α being the thermal expansion coefficient, and k is the thermal conductivity.

Finally, conservation of momentum implies that the rate of change of momentum must be equal to all forces acting on a given volume of the fluid mantle, namely surface forces (arising from viscous stresses) and body forces (due to gravity):

$$\rho \frac{d\mathbf{u}}{dt} = \boldsymbol{\nabla} \cdot \boldsymbol{\sigma} + \rho \mathrm{g} \tag{1.5}$$

where $\boldsymbol{\sigma}$ is the stress tensor and g is the gravity vector. This equation is simply Newton's second law of motion.

The total stress tensor $\boldsymbol{\sigma}$ is:

$$\boldsymbol{\sigma} = -P\boldsymbol{I} + \boldsymbol{\tau} \tag{1.6}$$

where P is the total pressure, $\boldsymbol{I}$ is the identity matrix, and $\boldsymbol{\tau}$ is the viscous or *deviatoric* stress tensor, which represents the non-hydrostatic component of stress. It is written in Einstein notation as:

$$\boldsymbol{\tau} = \tau_{ij} = \eta\left(u_{i,j} + u_{j,i} - \frac{2}{3}\delta_{ij}u_{k,k}\right) + \lambda\delta_{ij}u_{k,k} \tag{1.7}$$

where η is the effective viscosity, δ_{ij} is the identity tensor (i.e., $\delta_{ij} = 1$ for $i = j$, and $\delta_{ij} = 0$ for $i \neq j$), and λ is the second coefficient of viscosity.

Equation 1.6 can be used to rewrite the stress divergence term in the conservation of momentum (Equation 1.5):

$$\rho\frac{d\mathbf{u}}{dt} = (-\boldsymbol{\nabla}P + \boldsymbol{\nabla}\cdot\boldsymbol{\tau}) + \rho\mathrm{g} \tag{1.8}$$

Conservation of mass and momentum can together describe the flow field, given an equation of state $\rho(P,T)$:

$$\rho = \rho_0\left(1 - \alpha T_1 + K^{-1}P_1\right) \tag{1.9}$$

where $T_1 = T - T_0$ is the three-dimensional temperature perturbations, K^{-1} is the compressibility of the mantle material, and $P_1 = P - P_0$ represents the 3-D pressure perturbations. The term ρ_0 is a reference density given by the *hydrostatic reference state* of the mantle, where $\mathbf{u} = 0$. In this case, Equation 1.8 becomes:

$$\boldsymbol{\nabla}P_0 = \rho_0\mathrm{g} \tag{1.10}$$

where P_0 and ρ_0 are the reference hydrostatic pressure and density, respectively. Subtracting this equilibrium state from Equation 1.5, we obtain the dynamic equation of motion:

$$\rho\frac{d\mathbf{u}}{dt} = -\boldsymbol{\nabla}(\delta P) + \boldsymbol{\nabla}\cdot\boldsymbol{\tau} + (\delta\rho)\mathbf{g} \tag{1.11}$$

where δP and $\delta\rho$ represent pressure and density perturbations, respectively. The density perturbations $\delta\rho$ are determined from the equation of state (Equation 1.9) and therefore:

$$\delta\rho = \Big(\frac{\partial\rho}{\partial T}\Big)\delta T + \Big(\frac{\partial\rho}{\partial P}\Big)\delta P = -\alpha\rho_0\delta T + K^{-1}\rho_0\delta P \tag{1.12}$$

The last term will be ignored as compressibility does not make first-order contributions.

1.3.2 Simplifications to constitutive equations

A number of simplications can be made to the governing equations of Section 1.3.1. First of all, mantle convection occurs on a time scale many times longer than that of the local acoustic velocity. Thus, sound waves can be ruled out as possible solutions to the flow equations through the *anelastic liquid approximation*:

$$\boldsymbol{\nabla}\cdot(\rho\mathbf{u}) = 0 \tag{1.13}$$

in which the term $\frac{\partial\rho}{\partial t}$ has been ignored in the conservation of mass equation (Forte *et al.*, 2015). Furthermore, it is assumed that the density perturbations $\rho_1(r,\theta,\phi)$ do not make first-order contributions to the equations of conservation of mass and energy and can therefore be neglected.

Similarly, the time derivative of velocity $\frac{\partial u}{\partial t}$ in the conservation of momentum equation may be neglected due to the very high viscosity of mantle rocks. This is the *infinite Prandtl number approximation*, a limit at which fluid motion occurs slowly enough to neglect inertial effects.

The second viscosity coefficient λ in the viscous stress tensor τ_{ij} describes the energy dissipation associated with volume changes. Density changes arising from mantle flow occur on time scales much longer than the relaxation time of processes which restore thermal equilibrium, and the second viscosity coefficient λ in Equation 1.7 can therefore be ignored (Landau and Lifshitz, 1987), rendering the viscous stress tensor entirely deviatoric:

$$\tau_{ij} = \eta \left(u_{i,j} + u_{j,i} - \frac{2}{3}\delta_{ij}u_{k,k}\right) \tag{1.14}$$

Furthermore, many numerical models assume a linear Newtonian rheology for the whole mantle, meaning that the viscosity η depends on temperature and pressure (or depth) but not stress or strain rate. This approach simplifies the solving process but fails to accurately represent areas where nonlinear rheology may be present, such as subduction zones and other high-stress regions.

1.4 Presentation of the study

The dynamic nature of the Earth's mantle can be observed indirectly through its many expressions on the surface, such as tectonic plate motions and glacial isostatic adjustment. Mantle convection is governed by rheological laws and the partial differential equations outlined in Section 1.3.1. The third chapter will discuss the numerical methods used to solve these equations, with a heavy emphasis on ASPECT, a relatively new open-source code designed to solve thermal convection and similar mathematical problems.

This study will use ASPECT to investigate the impact of lateral viscosity variations on numerical simulations of mantle convection, and particularly their impact on calculations of dynamic topography. Together with the non-hydrostatic geoid, dynamic surface topography is one of the most important convection-related observables. Without mantle convection, the surface topography of the Earth would be entirely due to lateral variations in crustal thickness and density; in other words, to isostatic compensation of the crust. The direct contributions of mantle convection can be inferred by subtracting the isostatically compensated crustal signal from the total observed surface topography of the Earth. It is important to note that the accuracy of the resulting estimates depends entirely on the uncertainties present in the crustal model, which may be considerable.

CHAPTER II

LATERAL VARIATIONS IN MANTLE VISCOSITY:
A LITERATURE REVIEW

2.1 Introduction

In 1687, Isaac Newton introduced the term *defectus lubricitatis* to describe the internal resistance of a fluid, which he proposed was "proportional to the velocity with which the parts of the fluid are separated from one another" (Newton, 1729). This describes, in the parlance of modern fluid dynamics, the linear stress–strain relation of a Newtonian fluid. At the time, Newton was mainly concerned with disproving the physics of his predecessor, René Descartes, and specifically the vortex theory of planetary motions through a fluid ether. One century later, the hydraulic engineer Pierre du Buat studied the temperature dependence of viscosity, but the concept was not fully formalised until 1822, when Claude-Louis Navier introduced coefficients of viscosity into the equations of fluid motion (Jacobson, 1991).

Viscosity is a key parameter in the study of mantle convection, and inversions of geophysical data have indicated that the mantle's effective viscosity varies significantly with depth. The simplest numerical models assume an isoviscous mantle, but more realistic estimates of viscosity can be determined and employed using modern computational methods. Two-layer viscosity profiles allow for a rheological distinction between the upper and lower mantle, with a viscosity increase typically occurring near 670 km depth. This coincides with a seismic discontinuity and major phase change from spinel to silicate perovskite, and while the viscosity increase could be due to a change in grain size, this increase has also been detected as deep as 1200 km (Schubert *et al.*, 2004). Changes around this depth could be related to a progressive "dewatering" of perovskite (Rudolph *et al.*, 2015), the deformation behaviour of ferropericlase (Marquardt and Miyagi, 2015), or a different phenomenon entirely. These diverse possibilities speak to the extreme complexity of mantle rheology.

More elaborate viscosity profiles have been determined through joint inversions of data from post-glacial rebound, mineral physics experiments, and convection-related observables (Mitrovica and Forte, 2004; Steinberger and Calderwood, 2006). Generally, radial viscosity profiles are constrained in the top $\sim$1000 km of the mantle by Haskell's value of 10^{21} $\mathrm{Pa \cdot s}$, a robust early estimate of average mantle viscosity based on Fennoscandian post-glacial uplift (Haskell, 1935). Lateral viscosity variations (LVV) have only recently received serious consideration, and different studies have reached contradictory conclusions as to their significance and relevance in numerical models. The present chapter will present an overview of literature concerning lateral viscosity variations in the Earth's mantle.

2.2 Significance

The effective viscosity of the mantle has only rarely been accorded three-dimensional treatment, often reduced to simple depth layers or even a single value. Lateral viscosity variations are sometimes considered an unnecessary addition to global models of mantle convection, not least because their inclusion can dramatically increase simulation runtime and resource usage. There is also conflicting research as to whether convection-related observables can be adequately described in terms of a radial viscosity profile alone. Furthermore, constraints on mantle viscosity can be quite poor.

For instance, laboratory experiments on rock deformation are limited, requiring significant extrapolations to mantle conditions and generating large uncertainties in the process (Karato, 2010). Olivine, the most abundant and best-studied mineral of the upper mantle, remains so poorly constrained in terms of activation energy, activation volume, grain size, and water content as to allow for the vastly different constructions of upper-mantle viscosity, from essentially constant to linearly increasing in the shallow asthenosphere (King, 2016). From this perspective, LVV certainly do seem to make models unnecessarily complicated.

On a local scale, laterally homogeneous viscosity is often an unrealistic assumption, particularly around subduction zones. LVV have also increasingly been investigated in the context of glacial isostatic adjustment. Seismic tomography has indicated significant heterogeneities in the mantle beneath East and West Antarctica, which Kaufmann *et al.* (2005) proposed as a large temperature–viscosity difference due to a deep cratonic root under East Antarctica. Van der Wal *et al.* (2015) found that a 3D viscosity provides better fits to GPS uplift data and significantly affects the spatial pattern of uplift rate, and that low viscosities ($< 10^{19}$ $\mathrm{Pa \cdot s}$) in the mantle below West Antarctica make it very sensitive to recent changes in ice thickness.

Rogozhina (2008) has argued that, regardless of their apparent impact on the geoid and other observables, lateral viscosity variations are a necessary component of comprehensive mantle flow models. It has been shown that only lateral viscosity variations can excite mantle flow in such a way as to generate the toroidal component of surface plate motions (Forte *et al.*, 2015). Spherically symmetric models fail to produce a toroidal component similar in energy to the poloidal component of flow.

2.3 Treatment

Early studies involving LVV were carried out almost exclusively in 2D Cartesian geometry, and most numerical models have neglected them entirely. The reader is referred to Moucha *et al.* (2007) and Rogozhina (2008) for an overview of these early investigations.

Relatively few studies have explored LVV in the whole mantle. Kaban *et al.* (2014a) looked at the combined effect of whole-mantle LVV and weak plate boundaries (WPB). They found that both were necessary to explain certain features of the geoid and dynamic surface topography, but that the effect of WPB was more dominant by far. They cautioned that considering the effects of whole-mantle LVV or WPB separately could lead to erroneous results.

On the other hand, Moucha *et al.* (2007) found little effect from LVV on dynamic topography and the geoid, especially compared to uncertainties in published seismic tomography models. Austermann *et al.* (2015) found an impact on dynamic topography due to LVV, but only in terms of change over time. Neither of these studies considered WPB, although the latter employed a rigid (*no-slip*) surface boundary condition, which is locally valid for Antarctica.

Most studies have modelled LVV assuming that an Arrhenius-type temperature dependence is dominant. Ghosh *et al.* (2010) investigated LVV using two methods: assigning specific viscosity contrasts to tectonic regions, and calculating a temperature dependence given by:

$$\eta = \eta_0 \cdot \exp\left(E \cdot \Delta T\right) \tag{2.1}$$

where η_0 is the reference viscosity, E is a parameter controlling the strength of the temperature dependence, and $\Delta T = T_0 - T$ is the difference between the temperature and reference temperature T_0. They found that the pattern of dynamic topography was unchanged, but that the magnitude was affected by as much as 20%.

Petrunin *et al.* (2013) modelled LVV up to ~5 orders of magnitude and found a strong effect on mantle dynamics and the geoid. The authors obtained lateral temperature anomalies by applying a constant velocity–density scaling factor to the S40RTS seismic tomography model of Ritsema *et al.* (2011), and from there modelled strong LVV using a homologous temperature approach:

$$\eta(r,\theta,\phi) = A_0(r)\exp\left(E\frac{T_m(r)}{T_a(r)+\delta T(r,\theta,\phi)}\right) \tag{2.2}$$

where the melting temperature T_m was calculated using two different depth-dependent functions for the upper and lower mantle, T_a is the adiabatic temperature profile, temperature variations δT were derived from density anomalies using a depth-dependent thermal expansion coefficient, E is a scaling parameter, and $A_0(r)$ is a factor to keep the radial viscosity constant.

Ranalli (2001) modelled LVV in the whole mantle using lateral temperature variations from the seismic tomography model of Su *et al.* (1994), assuming the following relation between temperature anomalies ΔT and shear wave velocity v:

$$\Delta T = \frac{0.3}{\alpha}\frac{\Delta v}{v} \tag{2.3}$$

where the coefficient of thermal expansion α had a depth-varying distribution. Assuming a regime dominated by diffusion creep and constant strain rate or constant viscous dissipation power-law creep, rather than by constant stress power-law creep, LVV were found to vary from one to four orders of magnitude, being more pronounced in the uppermost and lowermost mantle.

Glišović *et al.* (2015) modelled grain size variability and found that lateral variations in grain size attenuate LVV. This work resulted in a new picture of LVV distribution through the whole mantle, while also revealing that traditional assumptions about temperature-dependent rheology in the lower mantle may be incorrect. Assuming that the upper mantle below 200 km could be modelled in terms of diffusion creep only, they used the experimentally determined flow law for dry olivine (Korenaga and Karato, 2008):

$$\eta_d = \frac{d^{m_1}}{A_1 \exp{(-\frac{E_1+pV_1}{RT})}} \tag{2.4}$$

where d is the grain size, m_1 is a grain-size sensitivity exponent, A_1 is a scaling constant, E_1 and V_1 are the activation energy and volume of dry olivine, p is the pressure, R is the ideal gas constant, and T is the temperature. The lower mantle was modelled in terms of vacancy diffusion for $MgSiO_3$ perovskite:

$$\eta_d = \frac{kd^2T}{AX_vVD_{pv}} \tag{2.5}$$

where k is Boltzmann's constant, A is a geometrical factor for modelling grain boundary sliding, X_v is the vacancy concentration, V is the molecular volume of perovskite, and D_{pv} is the effective diffusivity in perovskite that is controlled by Mg diffusion.

Glišović *et al.* (2015) varied the values of activation enthalpy for grain growth H_{gr} and for diffusion H. For $H_{gr}/H \leq 1$, they found complex LVV in the upper mantle and local regions of reduced viscosity in the middle lower mantle associated with hot upwellings. However, results from the $H_{gr}/H = 1.5$ model imply a counter-intuitive relationship between temperature and viscosity due to the strong effect of grain size. This model suggests that hot upwellings in the lower mantle could actually be stiffer than average due to larger grain sizes. Therefore, the traditional assumption of an Arrhenius-type temperature dependence for vacancy diffusion in the lower mantle may not be entirely valid.

The rheological impact of grain size and other microphysical parameters has also been investigated on a local scale. Barnhoorn *et al.* (2011) used both diffusion and dislocation flow laws for olivine to model the upper mantle beneath Scandinavia and found LVV up to 3-4 orders of magnitude, mainly due to large temperature anomalies present in the thermal data sets that were used (Goes *et al.*, 2000). Both dislocation and diffusion creep were identified as active deformation mechanisms in the upper mantle beneath Scandinavia on the time scale of glacial isostatic adjustment, and their relative contributions were found to be sensitive to microstructural parameters like grain size, water content, and stress levels present during deformation.

2.4 Conclusion

The dynamic impact of lateral viscosity variations remains poorly understood. However, it has been shown that spherically symmetric models are unable to produce a comprehensive picture of global mantle flow. In particular, LVV are necessary to excite the toroidal component of mantle flow (Forte *et al.*, 2015). To avoid incorrect results, care must be taken to investigate possible interactions between LVV and other conditions such as weak plate margins (Kaban *et al.*, 2014a).

The spatial distribution of LVV also remains unclear, though strong lateral heterogeneities are implied in the upper mantle, particularly in the lithosphere. Mantle rheology depends strongly on temperature, pressure, strain rate, and grain size; but many studies have calculated LVV assuming a simple Arrhenius temperature dependence. This could be a drastically invalid assumption for the lower mantle in particular (Glišović *et al.*, 2015). Ranalli (2001) has asserted that rheology of the transition zone and lower mantle will remain highly speculative until more is known about average grain sizes and the pressure dependence of creep in garnet and perovskite.

Direct modelling of LVV has been extremely limited until very recently. Continuing advances in high-performance computing and high-pressure mineral physics will enable ever more sophisticated numerical models and move us towards the development of a more complete description of mantle rheology.

CHAPTER III

COMPUTATIONAL GEODYNAMICS

3.1 Overview

Though partial differential equations can sometimes be solved without numerical methods, those that govern mantle convection generally require them. The field of computational geodynamics began to emerge around 1970, with the earliest one-dimensional models giving way to a flurry of two-dimensional investigations of subduction, thermal convection, and other topics (Gerya, 2010). The first three-dimensional mantle convection models appeared in the mid-to-late 1980s, and the field has since seen remarkable advances by virtue of increasing computing power.

Various numerical techniques have been developed to solve partial differential equations, including finite difference, finite element, finite volume, and spectral methods (Schubert *et al.*, 2004). The equations described in Section 1.3.1 apply to a continuum, or an infinite number of points, and thus present an infinite number of unknown variables. Quasi-analytical solutions can be obtained through the spectral and pseudo-spectral methods, but most numerical techniques obtain an approximate solution through *discretisation* of the original equations, which reduces them to a discrete problem with a finite number of unknowns (Johnson, 2009).

Many different codes exist to solve the problem of mantle convection, but this chapter will focus on the open-source code ASPECT, beginning with a brief overview of the finite difference and finite element methods, then explaining the inner workings of ASPECT while addressing its strengths as well as its shortcomings.

3.2 The finite difference method

The finite difference method obtains a discrete problem by replacing derivatives in the original equations with differences computed between two discrete points. For instance,

$$\frac{\partial A}{\partial x} = \frac{\Delta A}{\Delta x} = \frac{A_2 - A_1}{x_2 - x_1} \tag{3.1}$$

where $\Delta A = A_2 - A_1$ is the difference in function A between two points, which on the x-axis are separated by a distance $\Delta x = x_2 - x_1$. Since the original derivative implies an infinitesimal difference, shortening the distance between points x_1 and x_2 will increase the accuracy of the finite difference approximation (Gerya, 2010). The same approach can also approximate higher-order derivatives. In this way, partial differential equations are reduced to sets of linear equations of finite differences. These differences are calculated on a numerical mesh, which approximates the continuum with a finite number of points. The finite difference method typically uses a regular grid and solves the problem only at each nodal point; the method is thus ill-suited for problems involving complex geometry or boundary conditions, which motivated the development of other techniques.

3.3 The finite element method

The finite difference method attempts to solve the derivatives directly. By contrast, the finite element method (FEM) attempts to solve the integral form of a differential equation instead. The integral version is also known as the "weak formulation" because it allows for more potential solutions by relaxing certain requirements of the original equation, which is sometimes too rigorous to be solved. FEM discretises the domain into smaller pieces as well, but solves the problem over each such "finite element" to obtain a quasi-continuous solution. Accuracy and numerical stability can be major issues with FEM, but it can also handle complex geometries and material discontinuities far better than the finite difference method. This technique forms the backbone of mantle convection code like CitComS (Zhong *et al.*, 2000) and ASPECT.

3.4 ASPECT

ASPECT, short for *Advanced Solver for Problems in Earth's ConvecTion*, is an open-source code that employs finite elements to solve the equations governing thermal convection (Kronbichler *et al.*, 2012). The project mainly focuses on mantle dynamics of the Earth, but the code has a modular structure to accommodate a wide range of research interests. Simulations are controlled with input files in which parameters can be specified to dictate everything from the rheology and geometry of a model to the desired output variables. Users can modify the default parameters of existing models or implement extensions of the source code to suit their needs. Compositional fields are another key feature which enables the study and tracking of heterogeneities in the mantle.

ASPECT builds upon the sound infrastructure of the `deal.II` finite elements library, which in turn depends on `TRILINOS` for parallel linear algebra and `p4est` for parallel mesh handling. These projects are actively maintained and serve much broader communities than ASPECT alone, providing a solid foundation and allowing developers and contributors to focus on elements of geophysical interest.

3.4.1 Numerical framework

The `deal.II` finite elements library forms the backbone of ASPECT, providing functionality for adaptive meshes, parallel computing, and linear algebra solvers for the systems of equations that describe thermal convection. ASPECT requires that the library be compiled with `p4est` for distributed adaptive mesh support (Burstedde *et al.*, 2011) and `TRILINOS` for parallel linear algebra support (Heroux *et al.*, 2005).

ASPECT solves the same fundamental equations described in Section 1.3.1, but as a finite element code, it approximates the solutions using linear basis functions. For the Stokes system comprising the equations of mass and momentum conservation, these basis functions cannot be arbitrarily chosen due to the *Ladyzhenskaya–Babuška–Brezzi* (LBB) condition, which requires that the problem be well-posed. ASPECT fulfils this stability condition using a Taylor-Hood scheme in which the polynomial degree of the pressure basis functions is one less than that used for the velocity elements (Kronbichler *et al.*, 2012). By default, ASPECT employs quadratic elements for the velocity and linear elements for the pressure. This is far more computationally expensive than the lowest-element scheme, in which the pressures are piecewise constant and the velocities are piecewise linear, but using higher-order elements improves the numerical stability of the solver as well as the accuracy of the solution. ASPECT similarly uses quadratic elements for the temperature, but this polynomial degree can theoretically be reduced to save on computation time in studies where the temperature field is of little interest and does not affect the accuracy of the velocity and pressure fields.

Once the Stokes and temperature equations are fully discrete, each can take the form of a system of equations to be conditioned into a more tractable form and then solved through an iterative method. Iterative solvers work through a problem repeatedly, at each step using the previous solution as a new starting point until the final approximation converges towards the true solution within a specified error tolerance.

These systems are not always linear, however. For example, Heister *et al.* (2017) have acknowledged compressibility as one of the most challenging issues in the development of ASPECT, since the mass conservation equation is only linear for incompressible models. The compressible case contains extra terms which introduce nonlinearity that must be linearised and solved iteratively in order to obtain a solvable linear system. Choosing the appropriate solving schemes and preconditioners can be difficult, and every choice involves a certain amount of trade-off. This process is described in detail and quantified using benchmarks in Heister *et al.* (2017).

3.4.2 Models and parameters

The community has developed numerous models and benchmarks for users to explore and build upon, all of which are described in the manual (Bangerth *et al.*, 2016). Simple models, like thermal convection in a two-dimensional box, are a computationally inexpensive way to familiarise oneself with the code or to investigate specific features. For instance, the `Sinker with averaging` benchmark uses a circular density contrast within a two-dimensional box to demonstrate how material properties can be averaged to avoid sharp discontinuities which would place too much strain on the numerical solver.

Most parameters have a default value, so input files for simple models can be very short. Since the code works in two spatial dimensions by default, the following line would be required to specify three dimensions:

```
set Dimension = 3
```

The material model, which describes material parameters of the mantle such as viscosity and density, can be set with just a few lines:

```
subsection Material model
  set Model name = simple compressible
end
```

Without further specification, ASPECT will use default values for viscosity and any other available parameters. To illustrate a less generic input, the following lines could be included to specify a spherical geometry from the core-mantle boundary ($r_{CMB} =$ 3481 km) to the surface ($r_{surf} =$ 6371 km) with fixed boundary temperatures $T_{CMB} =$ 4000 K and $T_{surf} = 400$ K:

```
subsection Geometry model
  set Model name = spherical shell
  subsection Spherical shell
    set Inner radius = 3481000
    set Outer radius = 6371000
  end
end

subsection Boundary temperature model
  set Model name = spherical constant
  subsection Spherical constant
    set Inner temperature = 4000
    set Outer temperature = 400
  end
end
```

Along with the graphical solution and other requested outputs, ASPECT generates a file that lists all possible parameters, including the default values for those which were not specified—even if they were not used in the simulation—and extensive commentary for each line. This allows results to be easily reproduced and removes any confusion about which parameters produced a given solution.

3.4.3 Extensibility

The so-called cookbooks provided in the manual are an excellent starting point for new users, but most projects require a high degree of custom input and extensions to the source code. Fortunately, ASPECT was designed to be extensible, making it trivial to include custom code for the material description, initial conditions, geometry, graphical outputs, and so on. Custom files can be included without affecting the functionality of the original source code—although that, too, could be modified by advanced users wishing to alter the fundamental way in which ASPECT solves the basic equations.

3.4.4 Parallelism

ASPECT supports parallel computing, meaning that its work can be split into different tasks across multiple processing units. For instance, graphical solutions are generated by default as Visualization Toolkit Unstructured (VTU) files, a format that allows different processors to calculate the solution on different sections of the working mesh. These partial solutions can be easily collected into the full geometry, for instance by visualisation software like ParaView, without the need to communicate to a single processor which would write a single output.

Computing clusters are typically comprised of many nodes, machines which have sockets containing multiple cores, also known as processors or CPUs. Different computing tasks require different approaches to resource management. Some jobs require access to a node-specific resource, so using many cores on the same node would not increase performance—each task would still be stuck waiting for the same resource. Only spreading the job across cores on different nodes would remove this bottleneck. However, other jobs would be slowed down by such a configuration, since communication time between nodes can introduce significant delays (Hager and Gerhard, 2011).

Ideally, any code would run twice as fast after doubling the number of cores used, but real code requires that some work be done serially, and there is always a limit where performance no longer increases. Parallel code projects typically provide speedup charts to help users choose the most economical resource allocation for their jobs. These charts illustrate the relation between performance and cores used. No such resource exists in the ASPECT manual, likely due to the high degree of variability between simulations, but Heien *et al.* (2012) provide parallel performance data for a simple spherical shell model.

The efficiency of parallel code also depends on an even distribution of work among cores. When load balancing, ASPECT currently considers only the degrees of freedom (DOF), a number determined by the dimensions and refinement of the mesh, as well as the discretisation of the original equations. Performance is not optimised for tracer particles and other computationally expensive elements of the code, although it is possible to choose a strategy that adaptively refines the mesh according to tracer particle density, viscosity variability, or another relevant criterion. Nonetheless, one model with one million DOF could run for thirty minutes on 12 processors, while another with the same DOF could take hours on many more processors due to a more complex mantle rheology.

3.4.5 Adaptive mesh refinement

Numerical simulations can be calculated on an even mesh, but accurate solutions for mantle convection require a very fine resolution, which can be computationally expensive. ASPECT allows for adaptive mesh refinement (AMR), a process by which the numerical mesh can be locally refined and coarsened over time, or simply within the first time step. Typically, the user will want to refine areas of interest on the mesh, which may contain higher relative errors due to strong heterogeneities in the velocity field or other calculated parameters. The mesh can also be coarsened for regions where the solution is more homogeneous and has smaller relative errors. This uneven refinement can remain constant after the first time step, or it can be allowed to adapt over time as the solution evolves—following a subducting slab, for example.

ASPECT solves a problem on an initial mesh with uniform cell spacing defined by the `Initial global refinement` parameter. When the `Initial adaptive refinement` parameter is non-zero, the code then uses one or more refinement strategies to compute an error field and flags some fraction of cells for refinement or coarsening. For example, setting the parameter `Refinement fraction` to `0.5` will flag 50% of all cells for refinement, choosing those with the highest relative error. ASPECT currently implements strategies that can flag for different compositions; specified boundaries; spatial variabilities of the density, viscosity, or temperature; among others.

An adaptively refined mesh can achieve the same overall accuracy as a regular mesh that has been uniformly refined to the same highest resolution (Kronbichler *et al.*, 2012). Moreover, this method can be up to a thousand times faster. AMR thus represents one of the major strengths of ASPECT.

3.5 Conclusion

ASPECT is a relatively new open-source code with a mandate to provide an extensible code base for geodynamic research and a vision to create an open and participatory community of users and developers. Like its predecessor CitComS (Zhong *et al.*, 2000), ASPECT uses the finite element method to solve convection problems in the Earth's mantle and elsewhere.

ASPECT depends on a few external libraries, which can make the installation process more challenging than if it were self-contained. Care must be taken to ensure that each component has been compiled with the same software versions (e.g., CMake, OpenMPI). However, this dependence is also a strength, as the code is "freed of the mundane tasks" associated with implementing the finite element method, parallel linear algebra, and parallel adaptive meshes (Bangerth *et al.*, 2016). The underlying libraries each have their own specialised development communities, and ASPECT automatically benefits from any updates or improvements.

ASPECT itself receives frequent updates and new features, but its newness can also be a weakness. The code is not as well-documented as CitComS and other finite element codes, and it lacks certain important features. ASPECT does not calculate gravity self-consistently, and it lacks an output plugin for the geoid. However, it is possible to develop any number of custom modules due to the extensible nature of the code, and this is perhaps its greatest strength, together with adaptive mesh refinement, which allows complicated problems to be solved on a selectively refined mesh at a fraction of the runtime of a problem solved on a uniformly refined mesh.

CHAPTER IV

MODELLING WITH ASPECT

4.1 Introduction

ASPECT is an open-source code originally developed to simulate thermal convection in the Earth's mantle (Kronbichler *et al.*, 2012). However, its extensible structure allows for a wide range of research possibilities. Community members have studied topics as diverse as the geodynamic evolution of Mars (Zhang and O'Neill, 2016), dynamic topography change across Antarctica (Austermann *et al.*, 2015), subducting slabs with complex visco-plastic rheology (Fraters, 2014), and even inner core convection (Dannberg, 2016).

ASPECT was designed to supersede older mantle convection software like CitComS, which has not seen a major release since 2014. Indeed, it boasts many powerful modern features, chief among them its modular format, adaptive mesh refinement, and parallel processing capabilities.

The present study seeks to determine the impact of lateral viscosity variations on instantaneous mantle flow and resulting dynamic topography. Additionally, the consequences of using different seismic tomography models will be explored. Parallel performance testing was also carried out using a simplified version of the final model in order to determine approximate resource requirements.

4.2 Numerical model

In earlier builds of ASPECT, the only material model that could represent lateral viscosity variations in a compressible mantle was the `Steinberger model`, in which the material parameters are defined by mineral physics and the lateral viscosity variations are determined by a depth-dependent temperature prefactor H/nR, following the work of Steinberger and Calderwood (2006). This model was used extensively in the early development of this work, but it was later modified with custom code to adopt the physical parameters and values used by Glišović *et al.* (2012).

The mantle was modelled as a 3D spherical shell. The reference density is given by the Preliminary Reference Earth Model of Dziewoński and Anderson (1981). The crust and lithosphere were combined into a single layer 80 km thick with a constant value of $3.196561\ \mathrm{g \cdot cm^{-3}}$. This value conserves the same amount of mass and gravity as the original PREM model.

ASPECT does not currently implement any self-consistent gravity models, so a custom module was developed to generate a gravity profile satisfying Poisson's equation (Poirier, 2000):

$$g(r) = -\frac{GM(r)}{r^2} = -\frac{G}{r^2}\iiint_V \rho(r)\, r^2 \sin\phi \, dV = -\frac{4\pi G}{r^2}\int_0^r \rho(r)\, r^2\, dr \qquad (4.1)$$

where $G = 6.67 \times 10^{-8}\ \mathrm{m^3 \cdot kg^{-1} \cdot s^{-2}}$ is the universal gravitational constant, and M is the mass contained within a sphere of radius r and density $\rho(r)$. Equation 4.1 was numerically integrated to obtain a depth-dependent gravity profile, shown together with the PREM density profile in Figure 4.1.

Following Glišović *et al.* (2012), the thermal conductivity k was linearly interpolated between four different values specified at the surface, at depths of 80 km and 2650 km, and at the CMB. The resulting profile is shown in Figure 4.2. The thermal expansion coefficient α was defined at three different depths, linearly interpolated between the surface and 670 km depth, from which point it followed a density dependence to the core–mantle boundary. This profile is shown in Figure 4.3. Specific values are detailed in Table 4.1.

The effective viscosity was calculated assuming an Arrhenius-type temperature dependence and a Newtonian rheology for the whole mantle (Davies, 1980):

$$\eta = \eta_0 \cdot \exp(-\beta \cdot \Delta T) \tag{4.2}$$

where η_0 is the depth-dependent viscosity, defined by the geodynamically-inferred V2 profile of Forte *et al.* (2010), β is a free parameter controlling the strength of the lateral viscosity variations, and $\Delta T = T - T_a$ is the difference between temperature T and the adiabatic background temperature T_a. Figure 4.4 shows the depth-varying V2 profile.

4.2.1 Choice of tomography model

S40RTS, the seismic topography model of Ritsema *et al.* (2011), was used extensively in the development of this work, since it has been built into the source code of ASPECT. However, S40RTS uses only shear wave travel times and is based on PREM (Dziewoński and Anderson, 1981), which is transversely isotropic from the Mohorovičić discontinuity defined at 24.4 km down to the Lehmann discontinuity defined at 220 km. Kaban *et al.* (2014a) noted that many tomography models based on PREM indicate sharp seismic velocity contrasts around 220 km depth which are not observed globally. The authors suggested that this is an artefact of a model based purely on seismic velocities, and further warned that inverting these velocities can propagate error to the estimated temperature field.

Furthermore, early results in this work suggested a prominent mantle upwelling under Tahiti, some 30 degrees west of the East Pacific Rise (EPR). Conrad and Behn (2010) obtained similar results using the S20RTS tomography model of Ritsema *et al.* (1999)

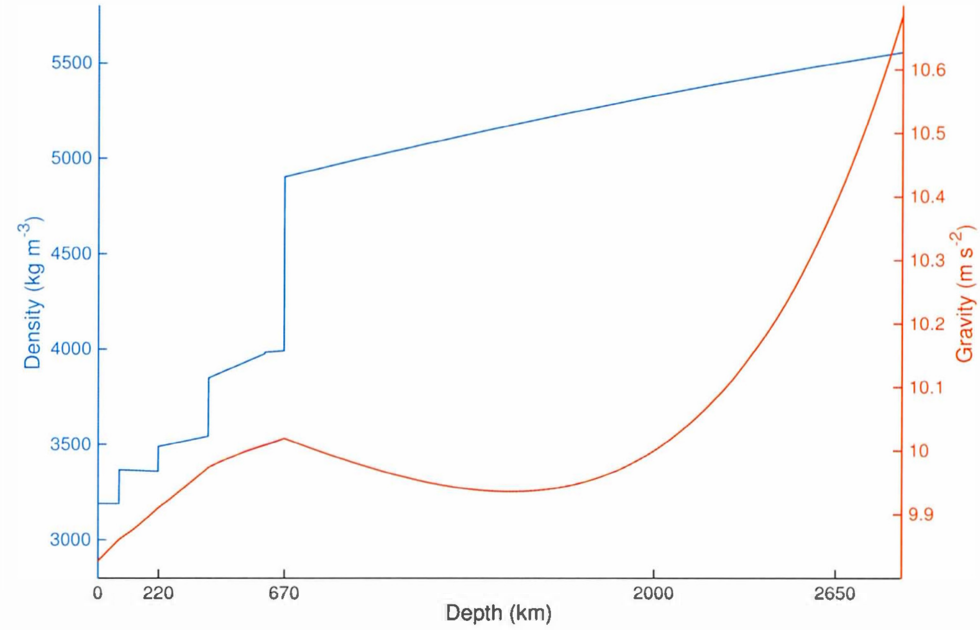

Figure 4.1: The depth-varying profiles of density and acceleration due to gravity used in the custom model, adapted from PREM (Dziewoński and Anderson, 1981).

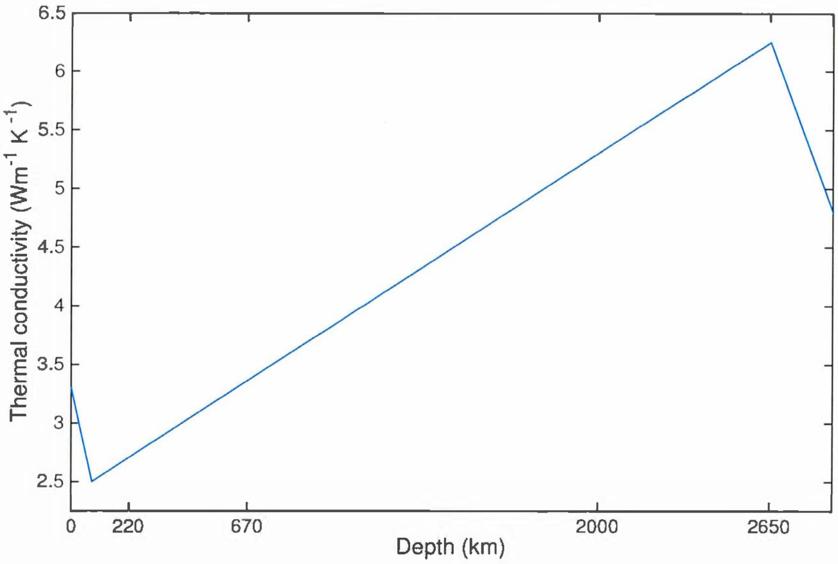

Figure 4.2: The depth-varying thermal conductivity k, from Glišović *et al.* (2012). Four values of k were assigned to depths of 0 km, 80 km, 2650 km, and 2888 km and then linearly interpolated.

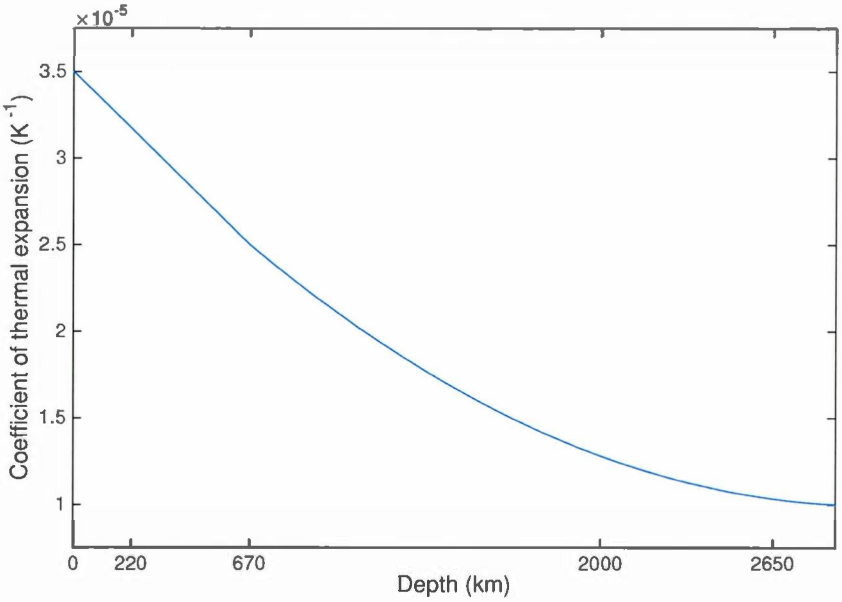

Figure 4.3: The depth-varying coefficient of thermal expansion α, from Glišović *et al.* (2012). The surface value of 3.5×10^{-5} K^{-1} decreases linearly to 2.5×10^{-5} K^{-1} at a depth of 670 km. From there, α decreases in a density-dependent manner to 1×10^{-5} K^{-1} at the CMB.

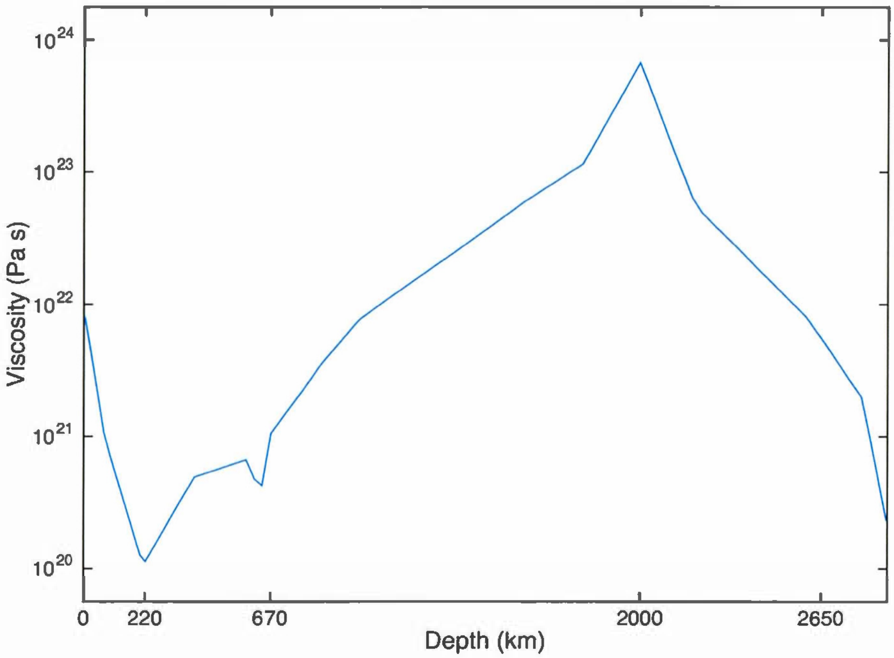

Figure 4.4: The depth-varying ‘V2’ viscosity profile (Forte *et al.*, 2010).

Outer shell radius	6368 km
Inner shell radius	3480 km
Adiabatic surface temperature	1700 K
Reference density	PREM
Reference viscosity	V2
Specific heat C_P	$1250\ \mathrm{J \cdot kg^{-1} \cdot K^{-1}}$
Thermal expansivity α (0 km)	$3.5 \times 10^{-5}\ \mathrm{K^{-1}}$
Thermal expansivity α (670 km)	$2.5 \times 10^{-5}\ \mathrm{K^{-1}}$
Thermal expansivity α (2888 km)	$1 \times 10^{-5}\ \mathrm{K^{-1}}$
Thermal conductivity k (0 km)	$3.3\ \mathrm{W \cdot m^{-1} \cdot K^{-1}}$
Thermal conductivity k (80 km)	$2.5\ \mathrm{W \cdot m^{-1} \cdot K^{-1}}$
Thermal conductivity k (2650 km)	$6.25\ \mathrm{W \cdot m^{-1} \cdot K^{-1}}$
Thermal conductivity k (2888 km)	$4.8\ \mathrm{W \cdot m^{-1} \cdot K^{-1}}$

Table 4.1: Parameters used in the custom model, with values adapted mainly from Glišović *et al.* (2012).

with a constant velocity–density conversion factor and concluded that large-scale mantle flow does not play a role in the spreading of the EPR. However, Rowley *et al.* (2016) argued that this westward shift arises from a purely seismic tomography model combined with constant velocity–density scaling. The authors found that the mantle flow rose directly below the EPR in simulations using TX2008, a more robust tomography model produced through a joint inversion of seismic and geodynamic data with additional constraints from mineral physics experiments (Simmons *et al.*, 2009). Furthermore, time-reversed simulations of mantle convection have shown a stable upwelling located under the EPR for at least the past 65 million years (Glišović and Forte, 2014).

Using geodynamic constraints, Rowley *et al.* (2016) determined a depth-dependent velocity–density scaling for S20RTS and found that, although the mantle upwelling retains a 30-degree shift westward of the EPR, the buoyancy of the lower mantle is greatly reduced. The authors concluded that even a depth-dependent scaling factor is insufficient to resolve this large-scale anomaly in the lower mantle. Their work underlines the critical importance of considering lateral variations in mantle structure.

To this end, the custom model was adjusted to use GyPSuM in lieu of S40RTS. GyPSuM provides mantle density perturbations based on a joint inversion of seismic body wave travel times and geodynamic observation data, with additional constraints from mineral physics (Simmons *et al.*, 2010). These density perturbations were converted to temperature anomalies and added to the background temperature shown in Figure 4.5—an adiabatic profile, since the temperature field cannot be calculated self-consistently by an instantaneous model.

The geodynamic consequences of using different seismic tomography models will be investigated and discussed. Although Rowley *et al.* (2016) compared results obtained using S20RTS and TX2008, the differences between S40RTS and GyPSuM are expected to be similar.

4.2.2 Boundary conditions

A well-posed problem requires boundary conditions to ensure a unique solution to a partial differential equation. For the spherical shell geometry, these limits are at the surface and core–mantle boundary.

Conservation of mass implies that the net mass flux must be zero across these boundaries. For simplicity, they are often modelled with either *free-slip* or *no-slip* conditions, which both require that the normal flow velocity is zero at the surface (i.e., $\mathbf{u}_\perp = 0$). Modelling them as deformable *free surfaces* is also possible, though usually computationally expensive.

A free-slip condition was applied to the CMB, allowing the mantle to flow laterally on this boundary. The surface was modelled as both a free-slip and no-slip boundary, with the latter requiring zero velocity on the boundary (i.e., $\mathbf{u}_\perp = \mathbf{u}_\| = 0$). This rigid condition does not correspond to a plate tectonics regime and is more applicable to planets like Venus and Mars.

4.2.3 Calculation of dynamic surface topography

Dynamic topography is the deflection of the Earth's surface in response to normal stresses arising from mantle flow. To calculate this deflection, ASPECT first computes the total normal stress at the level surface of the convection model:

$$\sigma_{rr} = -p_d + \hat{g}^T \left(\boldsymbol{\tau} \cdot \hat{g}\right) \tag{4.3}$$

where $p_d = p - p_a$ is the dynamic pressure calculated by subtracting the adiabatic pressure p_a from the total pressure p, $\hat{g} = \frac{\mathbf{g}}{\|\mathbf{g}\|}$ is the direction of the gravity vector g, and $\boldsymbol{\tau}$ is the viscous stress tensor.

The dynamic topography h is then given by:

$$h = \frac{\sigma_{rr}}{\Delta\rho\,\|\mathbf{g}\|} \tag{4.4}$$

where σ_{rr} is the total normal stress at the level surface of the convection model, given by Equation 4.3; and $\Delta\rho$ is the density contrast between the top of the model and a specified loading density. The definition of $\Delta\rho$ is an important one; the density contrast is much smaller for a crust loaded with seawater ($\rho_{sw} \approx 1025\ \mathrm{kg}\cdot\mathrm{m}^{-3}$) than with air ($\rho_{air} \approx 1\ \mathrm{kg}\cdot\mathrm{m}^{-3}$), which in turn will produce larger amplitudes in the calculated dynamic topography.

Topography would ideally be generated using a deformable free surface at the top boundary, but free surfaces are challenging to stabilise. Crameri *et al.* (2012) compared three different methods for calculating dynamic topography: using normal stress at the surface, using a free surface, and using "sticky air" as a free-surface approximation. The normal stress approach was shown to be accurate only if the resulting topography is small relative to the model dimensions and if the topography slopes are small. Furthermore, the method failed to predict the time-dependent relaxation into isostatic equilibrium, topography variations on time scales shorter than the isostatic relaxation time (t $\sim 10^4$ years), and the topography resulting from viscous plate bending. "Sticky air" uses a thin fluid layer with low density and viscosity to simulate a free air–crust interface. This was shown to be a good approximation to a true free surface, but only if the parameters were chosen carefully and with a stabilisation algorithm. ASPECT does not currently support a free surface in 3D spherical geometry. For simplicity, the normal stress method described by Equation 4.4 will be used.

This study will investigate water-loaded dynamic topography, with and without lateral viscosity variations, and with free-slip and no-slip boundary conditions at the surface.

4.2.4 Updated viscosity profile

It is important to isolate the impact of LVV from results which can be accounted for by an equivalent one-dimensional viscosity profile. In other words, the horizontally averaged viscosity must remain the same with or without LVV in order to make a proper comparison. Since the introduction of LVV can change the horizontally averaged viscosity, the model with LVV was completed first, and the horizontally averaged viscosity from this model was fed back into ASPECT as an "updated" radial viscosity profile for the model without LVV.

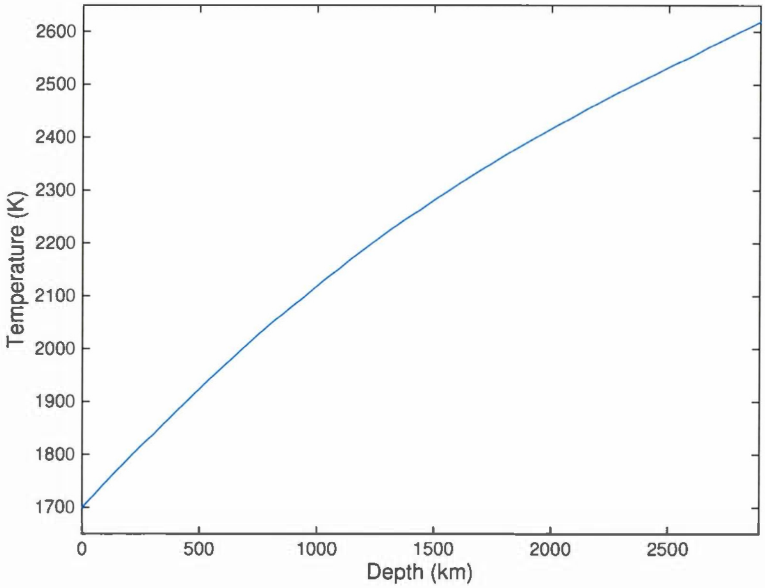

Figure 4.5: Adiabatic temperature profile with $T_{surf} = 1700$ K and $T_{cmb} = 2619$ K.

4.3 Results and discussion

4.3.1 Parallel performance

All performance testing was carried out on the University of Florida's HiPerGator 2.0 supercomputer (HPG2) using OpenMPI 1.10.2 for parallel computing and SLURM 15.08.9 to handle job submissions. Simulations were carried out on nodes with 32 cores each; their full specifications are outlined in Table 4.2.

Parallel jobs can fail, seemingly for no reason, when resource requests are poorly defined. Simply requesting n cores without further specifications can yield unpredictable configurations on some clusters, including HPG2: those n cores can be scattered unevenly across any number of available nodes. Additionally, there are known communication issues between OpenMPI and SLURM. Resource distribution was therefore clearly specified in each simulation to avoid ambiguity and obtain reliable runtime data.

Parallel performance decreases drastically as a fixed number of cores is spread across an increasing number of nodes. A simplified version of the model was computed in just 12 minutes using two full nodes, but the same model spread out evenly over four nodes timed out after two hours. Performance improved when the task load was assigned to just one of each node's two sockets (i.e., using all of the cores on one socket and none on the other), but the total runtime in this case was still unreasonably long: 74 minutes.

Although the HiPerGator 2.0 cluster is interconnected through InfiniBand networks, spreading out cores still creates barriers to efficient communication and memory access. An ideal parallel distribution would maximise communication between cores on the same socket of the same node and minimise communication between cores on different nodes, but this is not a simple task and depends significantly on the internal workings of ASPECT itself. For the purposes of this work, it is sufficient to choose a configuration that uses the least number of nodes while still accommodating the size of the problem (i.e., the degrees of freedom).

Before proceeding to actual simulations, the simplified model was run on 16, 32, 64, 128, 256, and 512 cores in order to estimate an ideal ratio between cores and degrees of freedom for a problem of this type. The results are presented in Figure 4.6. Each coloured line indicates the time consumed by a given step of the solving process. In order for ASPECT to obtain a solution meeting the specified error tolerance (10^{-5}), the Stokes and temperature systems were each built and solved four times.

These data can provide only a crude estimate of the parallel efficiency, since they do not reflect the final model's full complexity nor the impact of lateral viscosity variations on runtime. However, these results are comparable to those of Heien *et al.* (2012), who found strong parallel scaling up to 10^5 degrees of freedom per core (dof/core) using a spherical shell model, and a minimum runtime at 64 cores for a model with 2.57×10^6 degrees of freedom. These results would indicate an ideal ratio of about 5×10^4 dof/core. Though simplified, the model used in the present study contains more complexity than that of Heien *et al.* and demonstrated a minimum runtime with 128 cores and 1.67×10^6 degrees of freedom, or about 1×10^4 dof/core. Computing power is certainly wasted using a smaller ratio, as the runtime decreases only minimally and eventually even increases. This becomes a moot point in the final simulations, however, as higher mesh refinements generate 10^8 degrees of freedom or more while the study was limited to about 10^3 cores per run.

4.3.2 Instantaneous mantle flow

Figure 4.7 shows the results for instantaneous mantle flow with free-slip boundary conditions at four different depths: the asthenosphere (300 km), the bottom of the transition zone (650 km), the deep mantle (2000 km), and the top of the D″ layer (2680 km).

Sockets	2
Cores per socket	16
Total cores	32
Memory per core	4 GB
Total memory	128 GB

Table 4.2: Specifications for the HPG2 compute nodes used in the parallel performance tests.

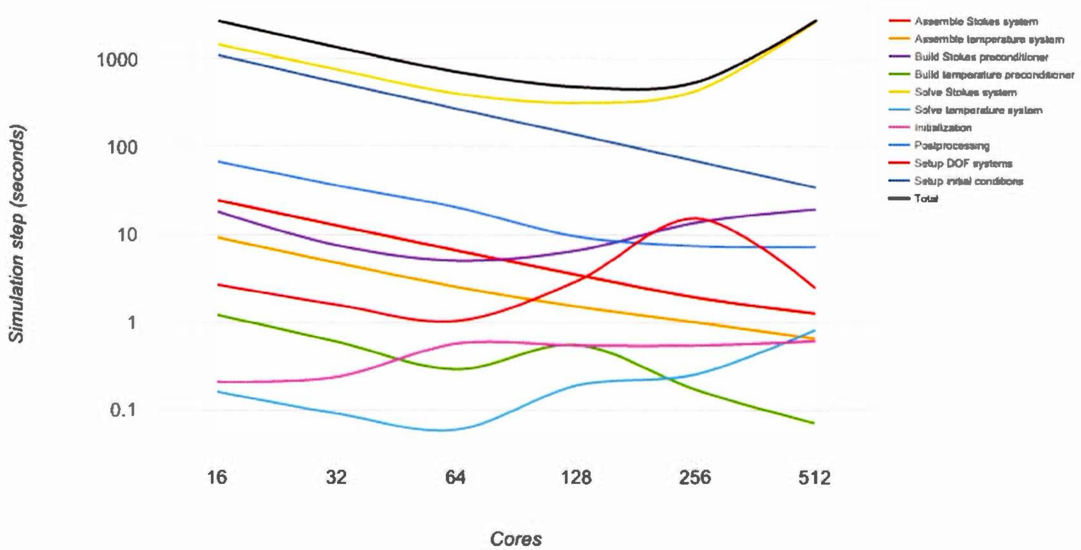

Figure 4.6: Parallel performance testing on the HPG2 supercomputer. A simplified version of the custom model with 1.67×10^6 degrees of freedom was run on 16, 32, 64, 128, 256, and 512 cores. The black line indicates the total runtime, while the coloured lines indicate the runtime for each specific simulation step.

The results for the model without LVV are reasonable and generally agree with published predictions (Forte *et al.*, 2015). The predicted mantle flow is more vigorous in the model with LVV, but the large-scale flow patterns do not change. This makes sense for a temperature-dependent model of LVV. However, the solver was unable to converge for $\beta > 0.01$ except with an unacceptably low mesh refinement and high error tolerance. Thus, only modest LVV spanning just 1-2 orders of magnitude could be modelled.

Figure 4.8 shows the horizontal surface divergence with and without LVV, as well as the radial vorticity induced by LVV. These results are superficially similar to those obtained by Moucha *et al.* (2007) and Rogozhina (2008), particularly the strong vortical flow east of Australia. Differences are likely due to the use of different methods and especially different seismic tomography models. The radial vorticity is zero in the absence of LVV. As previously discussed in Section 2.2, only LVV can generate toroidal flow comparable in energy to that of poloidal flow. Their inclusion is necessary for a comprehensive model of mantle convection.

Figure 4.9 shows the results for instantaneous mantle flow with a no-slip surface boundary condition at four different depths: the asthenosphere (300 km), the bottom of the transition zone (650 km), the deep mantle (2000 km), and the top of the D$''$ layer (2680 km). The free-slip condition has been subtracted to isolate the effect of a rigid surface. Comparing these to Figure 4.7, one can see that the rigid surface substantially reduces the flow velocities, especially in the upper mantle.

4.3.3 Dynamic surface topography

Figure 4.10 shows the dynamic surface topography calculated as per Equation 4.4 with no LVV and free-slip boundary conditions. The maximum and minimum amplitudes

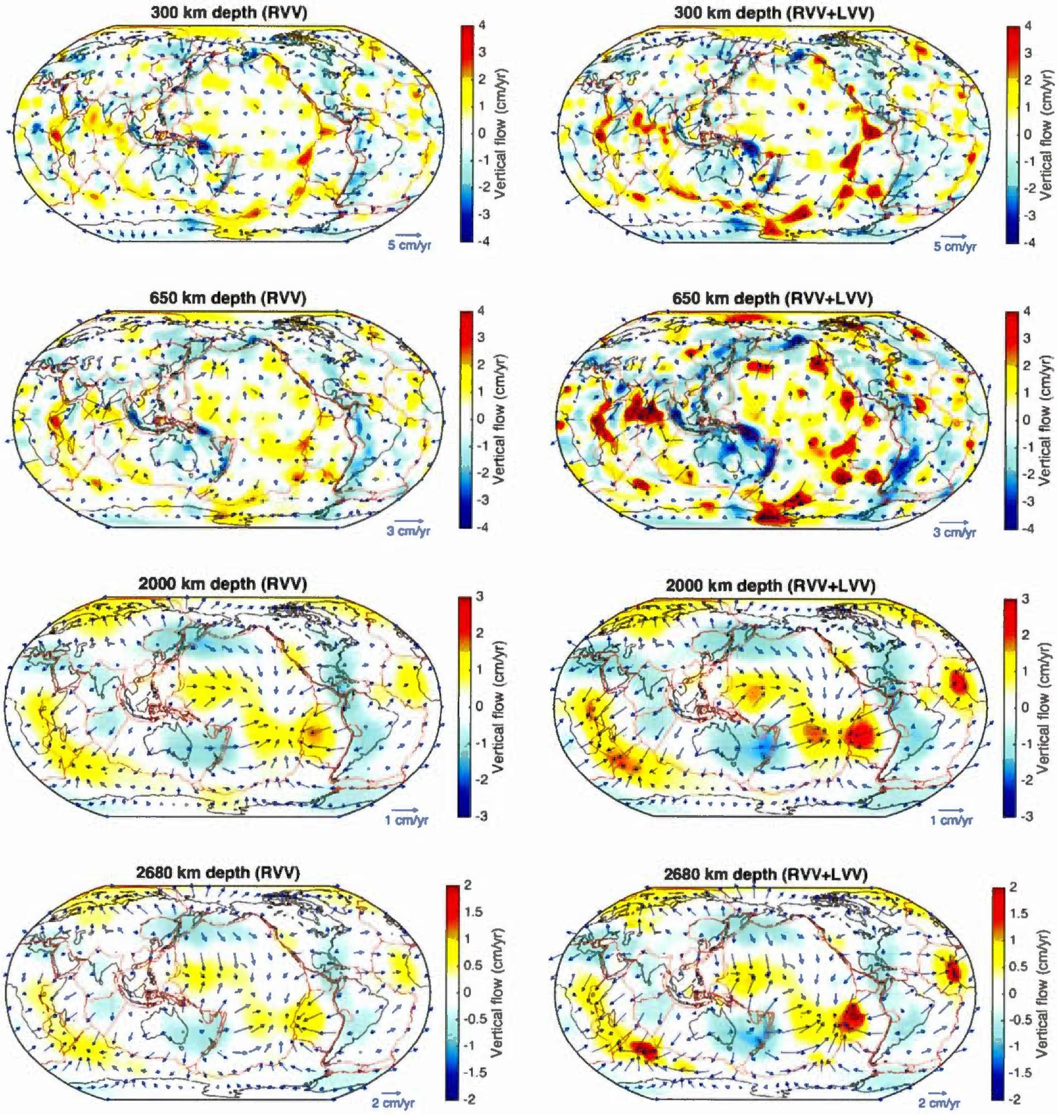

Figure 4.7: Predicted mantle flow with (right) and without (left) modest LVV and with a free-slip surface boundary condition.

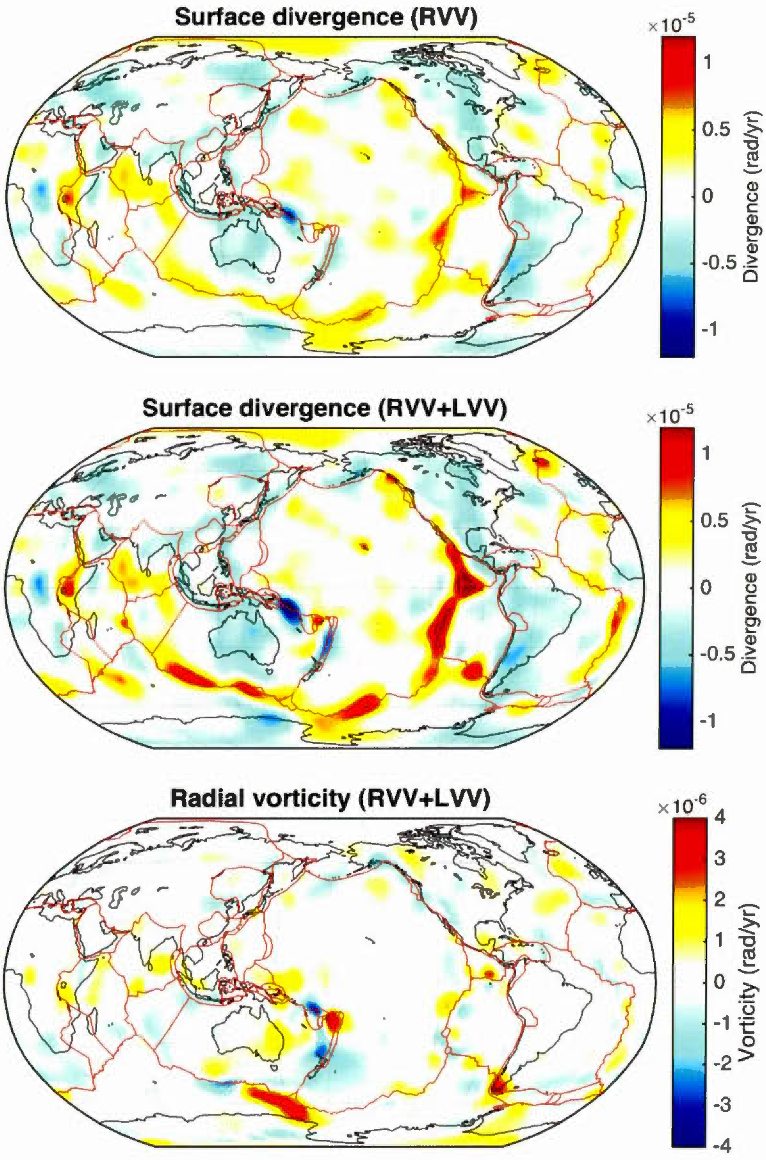

Figure 4.8: Calculated surface divergence without and with LVV, and calculated radial vorticity with LVV. Radial vorticity is zero in the absence of LVV.

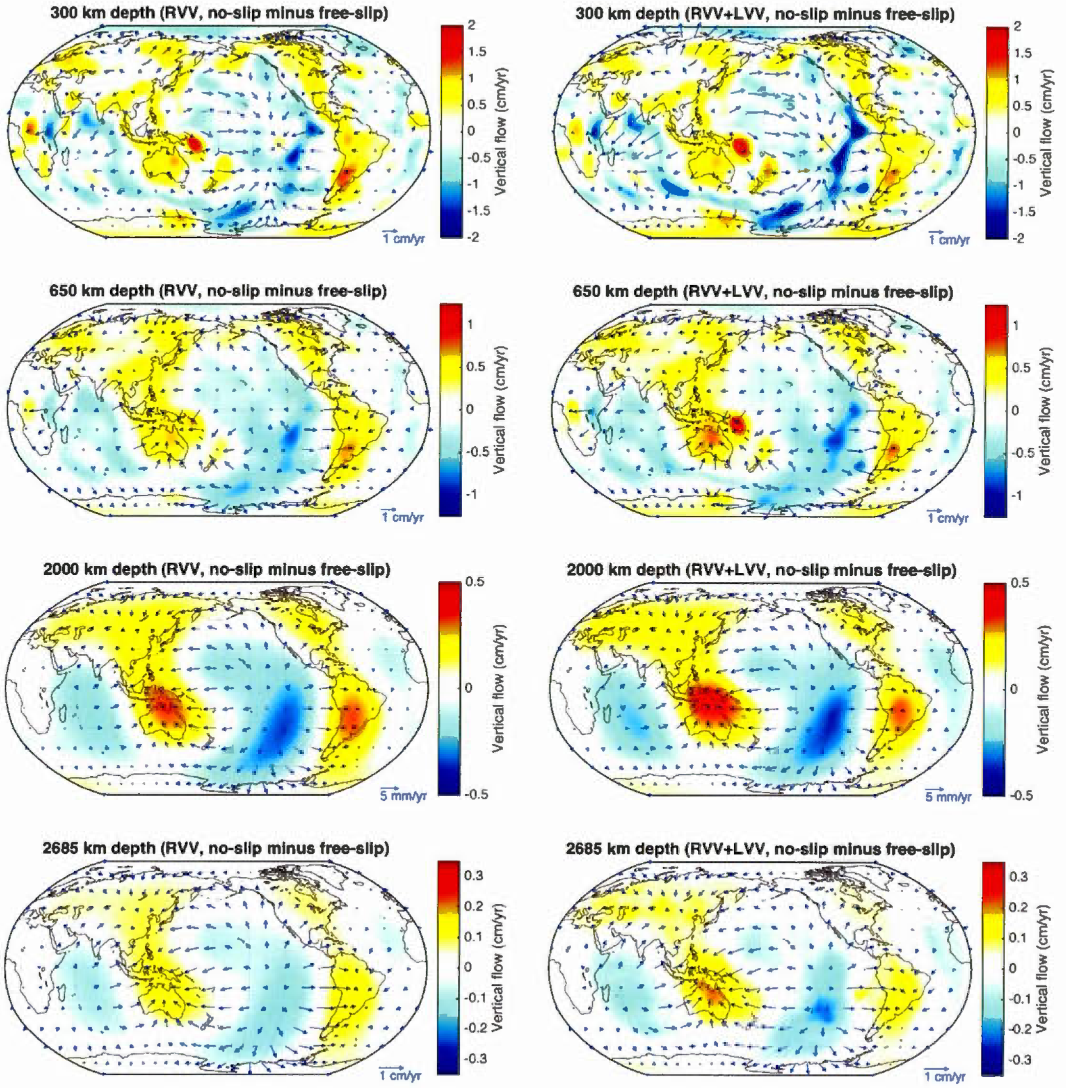

300 km depth (RVV, no-slip minus free-slip)

300 km depth (RVV+LVV, no-slip minus free-slip)

650 km depth (RVV, no-slip minus free-slip)

650 km depth (RVV+LVV, no-slip minus free-slip)

2000 km depth (RVV, no-slip minus free-slip)

2000 km depth (RVV+LVV, no-slip minus free-slip)

2685 km depth (RVV, no-slip minus free-slip)

2685 km depth (RVV+LVV, no-slip minus free-slip)

Figure 4.9: The impact of a no-slip surface condition on predicted mantle flow with (right) and without (left) modest LVV.

are 2.67 km and -1.74 km, respectively.

Figure 4.11 shows the impact of lateral viscosity variations on the dynamic surface topography. This result agrees with the findings of Kaban *et al.* (2014b), who found that weak plate margins and LVV tend to decrease the amplitude of positive dynamic topography around ridges and of negative dynamic topography associated with subduction zones. Kaban *et al.* (2014b) found, however, that WPB attenuated the dynamic topography significantly, and that LVV reduced this effect. Future work should therefore investigate the specific effect of weak plate margins.

Figure 4.12 shows the impact of a rigid boundary condition in the model without LVV. These results are sensible, as a no-slip boundary condition is supposed to generate more dynamic topography than free-slip due to added dissipation (Hager, 1991).

4.3.4 Importance of mesh resolution

Preliminary tests were run with the parameter `Initial global refinement` set to `3`, which yields `1,674,538` degrees of freedom and `49,152` active cells. This is already a large problem that requires multiple cores to run, but the horizontal resolution is relatively poor for a 3D whole-mantle simulation: only about 4° × 4°.

The developers suggest choosing an error tolerance low enough that the solution no longer changes, but this choice is limited by the resolution of the numerical mesh. Due to resource limits and the sheer size of the problem, the maximum resolution possible was `Initial global refinement = 5`, which yields `104,645,770` degrees of freedom and `3,145,728` active cells on 6 levels. However, even this level of mesh refinement is the bare minimum, at best, for computing an acceptable solution.

Figure 4.13 demonstrates the impact of increasing the `Initial global refinement`

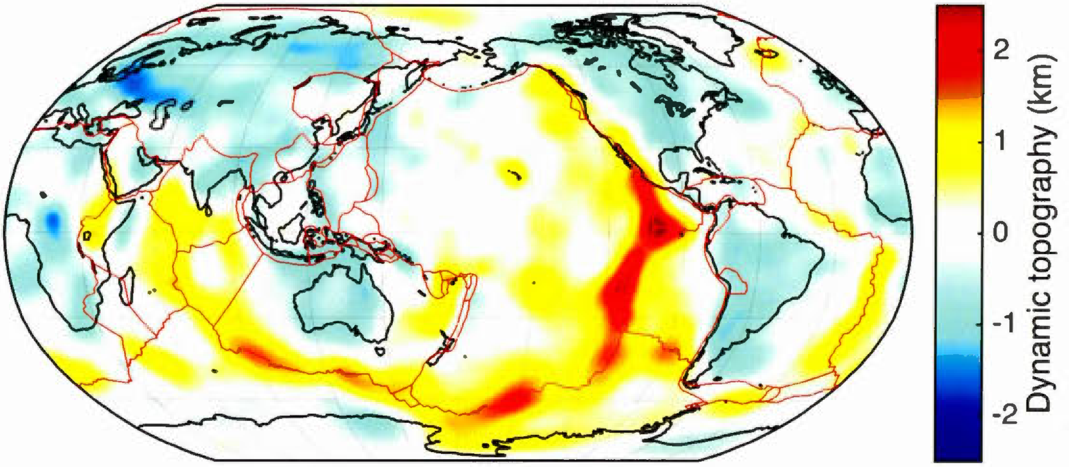

Figure 4.10: The dynamic surface topography produced according to Equation 4.4 and using a purely radial viscosity model.

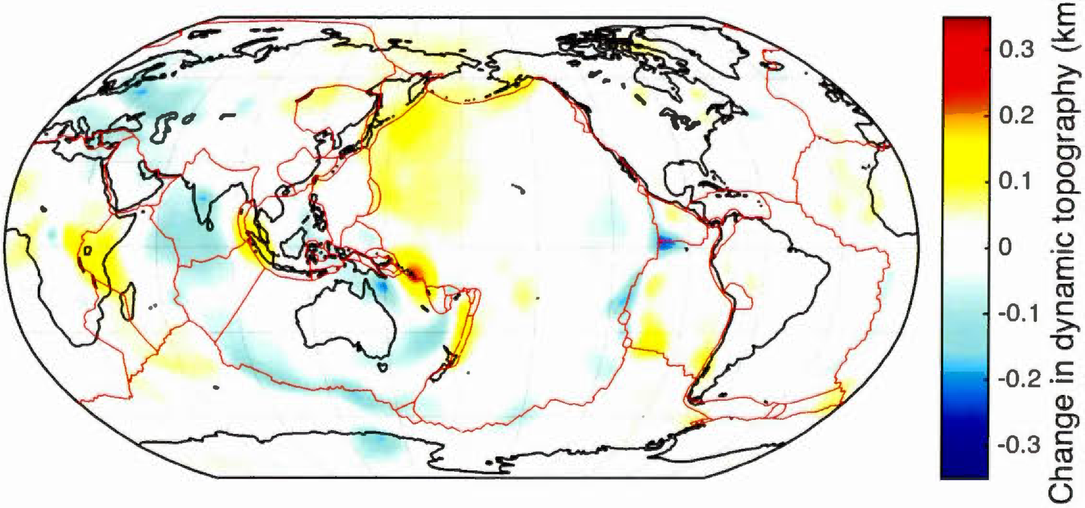

Figure 4.11: The changes in dynamic surface topography produced when modest LVV ($\beta = 0.01$) are added to the free-slip model.

parameter from 3 to 5. Although the overall pattern remains the same, there are several areas where the vertical flow changes by around $2\ \mathrm{cm} \cdot \mathrm{yr}^{-1}$. Figure 4.14 shows that the higher refinement level also increases the amplitude of the dynamic surface topography. The positive dynamic topography along multiple plate boundaries is increased by over 500 m. Both meshes are visualised in Figure 4.15.

This problem underlines the importance of adaptive mesh refinement, previously described in Section 3.4.5. Unfortunately, the adaptive refinement process can be difficult to implement with complicated models, since the problem size (degrees of freedom) can change by orders of magnitude. The workload can be redistributed among parallel processors, but the resources assigned to a run are fixed. The parallel performance testing of Section 4.3.1 revealed a limited window of solver functionality: it fails to converge when a large problem is spread across an unsuitable number of processors, whether too few or too many. Solving this issue is of critical importance to future work. Going forward, AMR functionality must be achieved to assure reasonable computation times and more efficient use of resources.

4.3.5 Choice of tomography model

Figure 4.16 shows the mantle flow fields at 300 km depth obtained with S40RTS and GyPSuM. This is a similar result to Rowley *et al.* (2016), in which S20RTS was found to suggest a mantle upwelling 30 degrees west of the East Pacific Rise, whereas the more robust TX2008 model predicted an upwelling directly beneath the EPR. This affirms the weakness of a mantle density model that relies on shear wave velocities alone and does not utilise 3D density–velocity scaling.

GyPSuM draws from geodynamic data, mineral physics, and seismic body wave travel times to create an extremely robust model of the Earth's mantle. The model also contains information about thermal and compositional contributions to variations in mantle density—a strong point that was not explored in this work. This study has assumed that compositional effects are negligible for the whole mantle, which is not always realistic. Simmons *et al.* (2010) argued that most of the mantle's density variations can be described in terms of thermal contributions alone, except for the upper and lowermost regions. Kaban *et al.* (2003) found that compositional differences (mainly iron depletion) account for about 40% of density variations under cratons. The non-cratonic upper mantle does not share this compositional signature, requiring a laterally variable treatment of the upper mantle. This work has described the mantle's density variations in terms of temperature differences alone, relating the anomalies in terms of a thermal expansion coefficient that varies with depth (see Table 4.1). Future developments should consider the complete thermochemical origin of mantle density anomalies, particularly in the case of time-dependent mantle dynamics. Fortunately, ASPECT has provided functionality for compositional fields from the beginning.

This unrealistic assumption has implications for the viscosity, which has been defined here as temperature-dependent. For parts of the upper and lower mantle, these variations represent a kind of "pseudo-temperature" that incorporates strong compositional effects. The viscosity itself has been grossly simplified, although V2 is a very robust radial viscosity model and simple temperature dependence is a common approach to modelling LVV. The effective viscosity may have a strong dependence on mineral grain size, particularly in the deep mantle where diffusion creep dominates (Glišović *et al.*, 2015). Variable composition affects viscosity as well; this effect in the lower mantle was recently investigated by Ballmer *et al.* (2017). These effects should be considered in later studies.

4.4 Conclusion

ASPECT was designed to reflect a new generation of numerical modelling, and it certainly has many strengths: a modular structure which can accommodate diverse research interests; an active community of developers and contributors; and implementation of modern numerical techniques, like adaptive mesh refinement. However, the code is an ongoing community effort and remains experimental in a few key areas, and fully realistic models of the whole Earth are still difficult to achieve. Code developers have acknowledged these limitations and worked to address issues like compressibility (Heister *et al.*, 2017).

This research has used ASPECT to investigate the impact of lateral viscosity variations on mantle flow and dynamic surface topography. The results suggest that LVV increase the vigour of mantle flow and decrease the amplitude of dynamic surface topography. However, these findings are somewhat inconclusive due to the small amplitude of the LVV. Solutions with strong LVV were achieved only at a low resolution and high error tolerance. The following section will provide final conclusions and recommendations for future research.

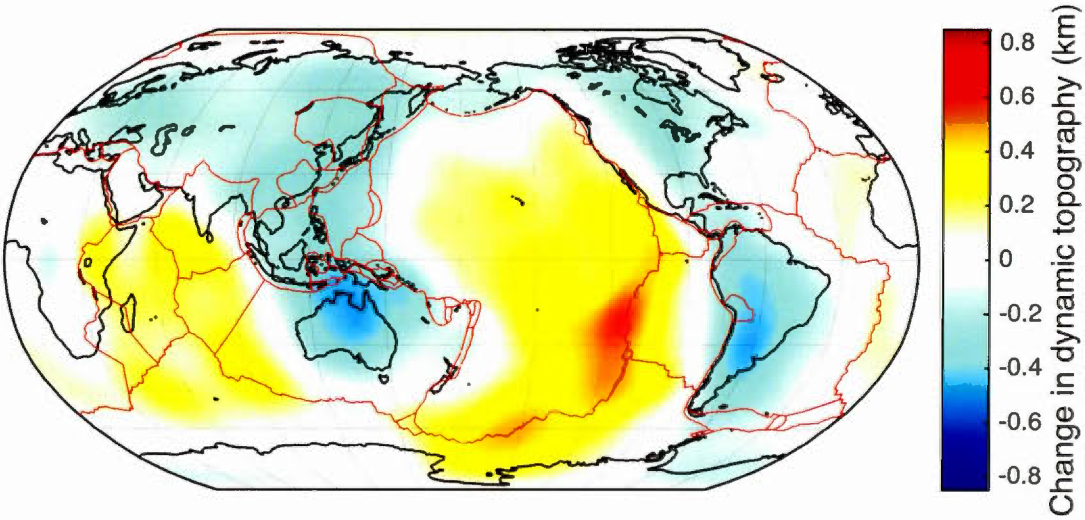

Figure 4.12: The impact of a rigid surface condition on the dynamic topography for a purely radial viscosity model.

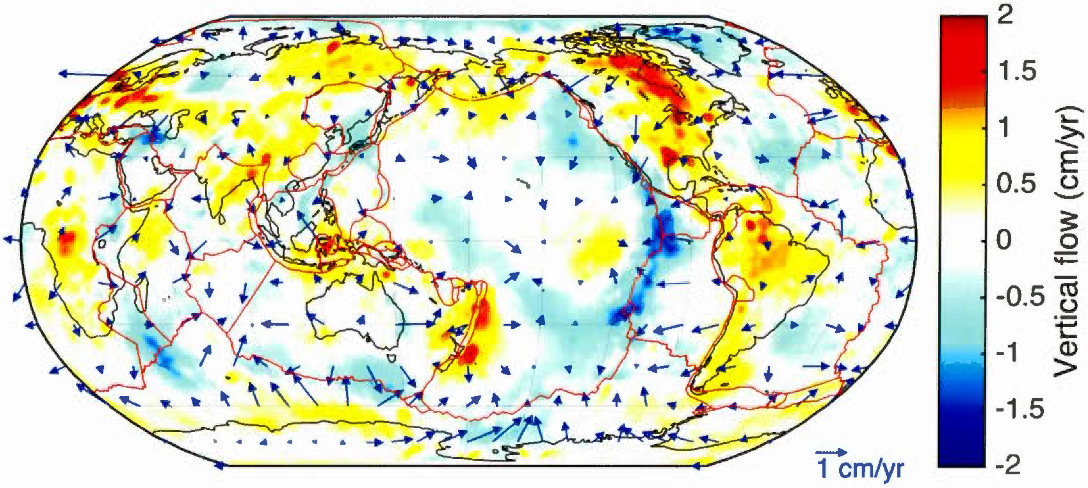

Figure 4.13: The impact of setting the parameter `Initial global refinement` to `5` compared to `3`. This figure shows the differential flow field at 300 km depth with free-slip boundary conditions and without lateral viscosity variations.

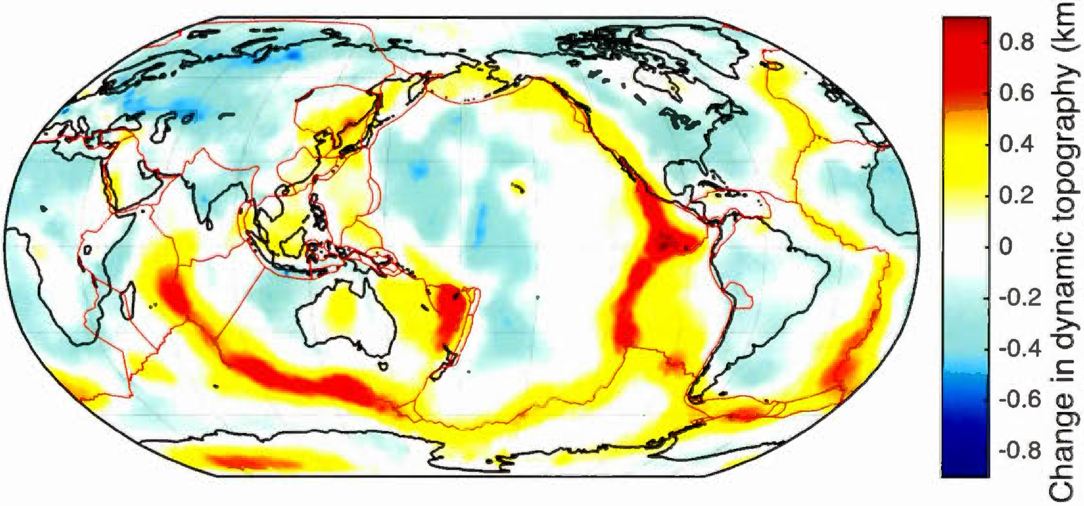

Figure 4.14: The impact of setting the parameter `Initial global refinement` to `5` compared to `3`. This figure shows the differential dynamic surface topography with free-slip boundary conditions and without lateral viscosity variations.

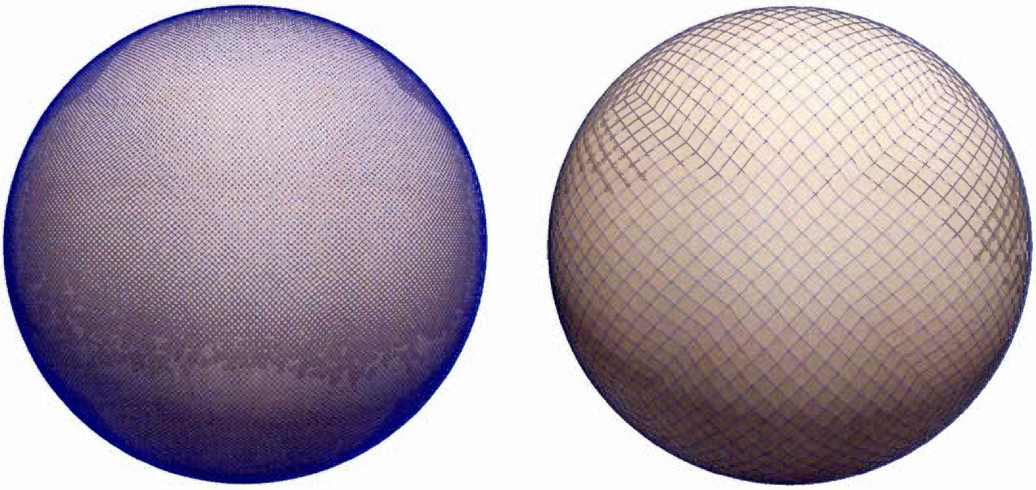

Figure 4.15: The 3D mesh with the parameter `Initial global refinement` set to `5` (left) compared to `3` (right).

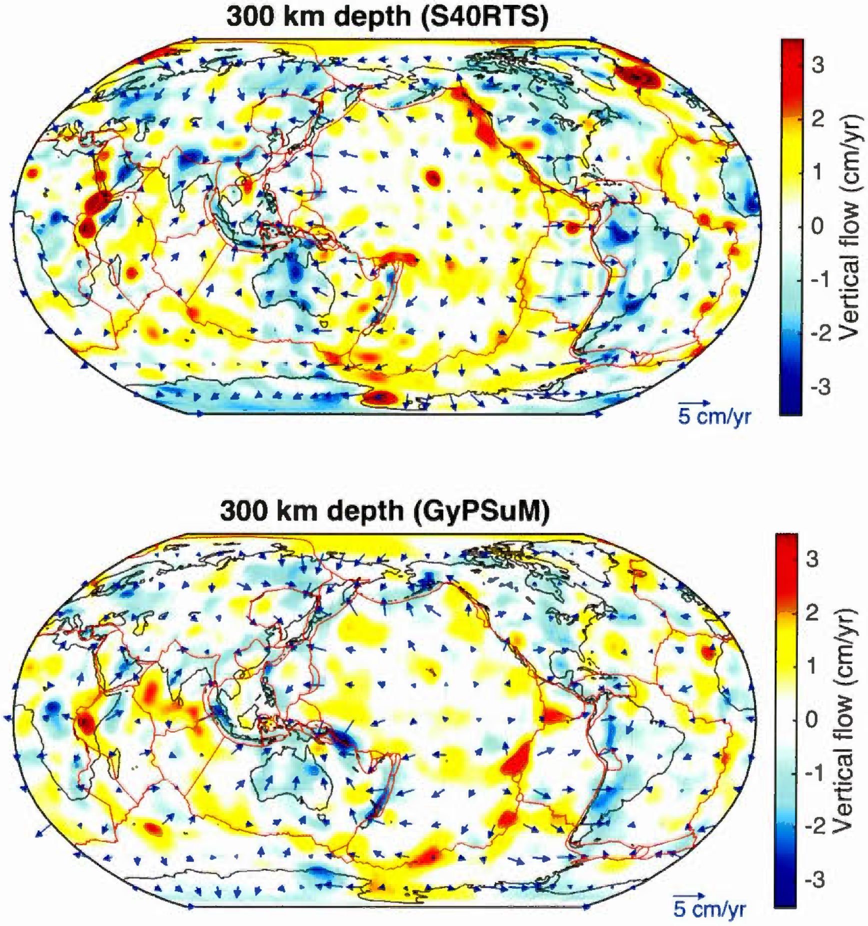
300 km depth (S40RTS)

300 km depth (GyPSuM)

Figure 4.16: Predicted mantle flow at 300 km depth using the GyPSuM (bottom) and S40RTS (top) seismic tomography models. S40RTS produces an apparent upwelling about 30 degrees west of the EPR.

CONCLUSION

The open-source mantle convection code ASPECT (Kronbichler *et al.*, 2012) has been used to model lateral variations in viscosity (LVV) in the Earth's mantle. The effective viscosity was calculated according to an Arrhenius-type equation for temperature dependence, with temperature perturbations given by the joint tomographic model GyPSuM (Simmons *et al.*, 2010) and a depth-varying reference viscosity given by the 'V2' profile (Forte *et al.*, 2010). The results suggest that LVV increase the vigour of mantle flow and reduce the amplitude of dynamic surface topography, but only small LVV spanning 1-2 orders of magnitude could be implemented. Further development with ASPECT is recommended.

The geodynamic implications of using different seismic tomography models have also been investigated. Comparisons between GyPSuM and S40RTS (Ritsema *et al.*, 2011) confirm earlier findings by Rowley *et al.* (2016) that shear-wave velocities are not sufficient to characterise the complex and three-dimensional structure of the Earth's mantle. Furthermore, the constant density–velocity scaling currently employed by the S40RTS model in ASPECT is not appropriate, nor even can a depth-varying scaling resolve the strong 3D heterogeneities in the lower mantle. Seismic tomography models should therefore contain independent constraints (e.g., from geodynamic data) and lateral variations in density–velocity scaling.

Dynamic topography is an important surface observable that can be estimated by subtracting isostatically compensated crustal heterogeneities from the total surface topography of the Earth. Many numerical models, including this study, calculate the dynamic topography using the total normal stress at a vertically fixed surface, which might fail to predict, for example, topography resulting from viscous plate bending (Crameri *et al.*, 2012). ASPECT does not currently support a free surface in 3-D spherical geometry, but it may be appropriate to implement or test the efficacy of a "sticky-air" free surface approximation.

This study has relied on a few unrealistic simplifications, including that mantle density anomalies are purely thermal in origin. Future work must consider the compositional signatures of the cratonic lithosphere and lowermost mantle. Furthermore, little consideration has been given to the crust and tectonic plates, but weak plate margins may strongly influence dynamic surface topography. Fraters (2014) used ASPECT to incorporate a lithospheric weak zone in a 2D subduction model but encountered issues with runtime and numerical stability. These issues will likely be resolved as the development of ASPECT moves towards accommodating more realistic descriptions of the mantle. Additionally, this study has modelled LVV considering only the temperature dependence of silicate rheology. However, grain size has been shown to have a comparable effect to that of temperature and pressure on mantle viscosity (e.g., Glišović *et al.*, 2015. Future work should incorporate these results.

ASPECT has been shown to have certain limitations, especially with respect to 3-D spherical geometry, compressibility, and large viscosity contrasts. However, recent developments have been made towards improving the nonlinear solver to better accommodate more realistic models, in particular those incorporating compressibility and melting (e.g., Heister *et al.*, 2017). Future work with ASPECT should focus on the use of adaptive mesh refinement to reduce computation time and allow some of the previously mentioned recommendations to be implemented.

BIBLIOGRAPHY

Anderson, D. L. and Minster, J. B. (1979). The frequency dependence of Q in the Earth and implications for mantle rheology and Chandler wobble. *Geophys. J. Int.*, *58*(2), 431–440.

Austermann, J., Pollard, D., Mitrovica, J. X., Moucha, R., Forte, A. M., DeConto, R. M., Rowley, D. B. and Raymo, M. E. (2015). The impact of dynamic topography change on Antarctic ice sheet stability during the mid-Pliocene warm period. *Geology*, *43*(10), 927–930.

Ballmer, M. D., Houser, C., Hemlund, J. W., Wentzcovitch, R. M. and Hirose, K. (2017). Persistence of strong silica-enriched domains in the Earth's lower mantle. *Nat. Geosci.*, *10*, 236–240.

Bangerth, W., Dannberg, J., Gassmöller, R., Heister, T. *et al.* (2016). ASPECT*: Advanced Solver for Problems in Earth's ConvecTion.* Computational Infrastructure in Geodynamics.

Barnhoorn, A., van der Wal, W., Vermeersen, B. L. A. and Drury, M. R. (2011). Lateral, radial, and temporal variations in upper mantle viscosity and rheology under Scandinavia. *Geochem. Geophys. Geosyst.*, *12*(1), Q01007.

Barton, C. (2002). Marie Tharp, oceanographic cartographer, and her contributions to the revolution in the earth sciences. *Geol. Soc. Lond. Spec. Publ.*, *192*, 215–228.

Becker, T. W., Kustowski, B. and Ekström, G. (2008). Radial seismic anisotropy as a constraint for upper mantle rheology. *Earth Planet. Sci. Lett.*, *267*(1–2), 213–227.

Benioff, H., Press, F. and Smith, S. (1961). Excitation of the free oscillations of the Earth by earthquakes. *J. Geophys. Res.*, *66*(2), 605–619.

Burstedde, C., Wilcox, L. C. and Ghattas, O. (2011). `p4est`: Scalable algorithms for parallel adaptive mesh refinement on forests of octrees. *SIAM J. Sci. Comput.*, *33*(3), 1103–1133.

Conrad, C. P. and Behn, M. D. (2010). Constraints on lithosphere net rotation and asthenospheric viscosity from global mantle flow models and seismic anisotropy. *Geochem. Geophys. Geosyst.*, *11*, 1525–2027.

Crameri, F., Schmeling, H., Golabek, G. J., Duretz, T., Orendt, R., Buiter, S. J. H., May, D. A., Kaus, B. J. P., Gerya, T. V. and Tackley, P. J. (2012). A comparison of numerical surface topography calculations in geodynamic modelling: an evaluation of the 'sticky air' method. *Geophys. J. Int.*, *189*(1), 38–54.

Dannberg, J. (2016). Inner core convection. In ASPECT*: Advanced Solver for Problems in Earth's ConvecTion* 144–149. Computational Infrastructure in Geodynamics.

Davies, G. F. (1980). Thermal histories of convective Earth models and constraints on radiogenic heat production in the Earth. *J. Geophys. Res.*, *85*(B5), 2517–2530.

Davies, G. F. (2000). *Dynamic Earth: Plates, Plumes and Mantle Convection.* Cambridge University Press.

Dietz, R. S. (1961). Continent and ocean basin evolution by spreading of the sea floor. *Nature*, *190*, 854–857.

Dziewoński, A. M. and Anderson, D. L. (1981). Preliminary reference Earth model. *Phys. Earth Planet. Inter.*, *25*, 297–356.

Forte, A. M. (2014). Géophysique globale: notes de cours SCT-8341. Université du Québec à Montréal.

Forte, A. M., Quéré, S., Moucha, R., Simmons, N. A., Grand, S. P., Mitrovica, J. X. and Rowley, D. B. (2010). Joint seismic–geodynamic–mineral physical modelling of African geodynamics: A reconciliation of deep-mantle convection with surface geophysical constraints. *Earth Planet. Sci. Lett.*, *295*, 329–341.

Forte, A. M., Simmons, N. A. and Grand, S. P. (2015). Constraints on 3-D seismic models from global geodynamic observables: Implications for the global mantle convective flow. In G. Schubert, B. Romanowicz, and A. M. Dziewoński (ed.), *Deep Earth Seismology*, volume 1 of *Treatise on Geophysics* chapter 27, 853–907. New York: Elsevier, (2 ed.).

Fraters, M. R. T. (2014). *Thermo-mechanically coupled subduction modelling with ASPECT.* (Unpublished master's thesis). Utrecht University.

Gerya, T. V. (2010). *Introduction to Numerical Geodynamic Modelling.* New York: Cambridge University Press.

Ghosh, A., Becker, T. W. and Zhong, S. (2010). Effect of lateral viscosity variations on the geoid. *Geophys. Res. Lett.*, *37*, L01301.

Glišović, P. and Forte, A. M. (2014). Reconstructing the Cenozoic evolution of the mantle: Implications for mantle plume dynamics under the Pacific and Indian plates. *Earth Planet. Sci. Lett.*, *390*, 146–156.

Glišović, P., Forte, A. M. and Ammann, M. W. (2015). Variations in grain size and viscosity based on vacancy diffusion in minerals, seismic tomography, and geodynamically inferred mantle rheology. *Geophys. Res. Lett.*, *42*(15), 6278–6286.

Glišović, P., Forte, A. M. and Moucha, R. (2012). Time-dependent convection models of mantle thermal structure constrained by seismic tomography and geodynamics: implications for mantle plume dynamics and CMB heat flux. *Geophys. J. Int.*, *190*(2), 785–815.

Goes, S., Govers, R. and Vacher, P. (2000). Shallow mantle temperatures under Europe from P and S wave tomography. *J. Geophys. Res.*, *105*, 11153–11169.

Hager, B. H. (1991). Mantle viscosity: A comparison of models from postglacial rebound and from the geoid, plate driving forces, and advected heat flux. In R. Sabadini, K. Lambeck, and E. Boschi (ed.), *Glacial Isostasy, Sea-Level and Mantle Rheology* 493–513. Boston: Kluwer Academic Publishers.

Hager, G. and Gerhard, W. (2011). *Introduction to High Performance Computing for Scientists and Engineers*. Boca Raton, FL: CRC Press.

Haskell, N. A. (1935). The motion of a viscous fluid under a surface load. *Physics*, *6*, 265–269.

Heien, E. M., Heister, T., Bangerth, W. and Kellogg, L. H. (2012). An analysis of ASPECT mantle convection simulator performance and benchmark comparisons. In *AGU (American Geophysical Union) Fall Meeting*.

Heister, T., Dannberg, J., Gassmöller, R. and Bangerth, W. (2017). High accuracy mantle convection simulation through modern numerical methods. II: realistic models and problems. *Geophys. J. Int.*, *210*(2), 833–851.

Heroux, M. A., Bartlett, R. A., Howle, V. E., Hoekstra, R. J., Hu, J. J., Kolda, T. G., Lehoucq, R. B., Long, K. R., Pawlowski, R. P., Phipps, E. T., Salinger, A. G., Thornquist, H. K., Tuminaro, R. S., Willenbring, J. M., Williams, A. and Stanley, K. S. (2005). An overview of the Trilinos project. *ACM Trans. Math. Softw.*, *31*(3), 397–423.

Hess, H. H. (1962). History of ocean basins. In A. Engel, H. L. James, and B. F. Leonard (ed.), *Petrologic Studies: A Volume to Honor A. F. Buddington* 599–620. Boulder, CO: Geological Society of America.

Jacobson, B. O. (1991). *Rheology and Elastohydrodynamic Lubrication*, volume 19 of *Tribology Series*. Amsterdam: Elsevier.

Johnson, C. (2009). *Numerical Solution of Partial Differential Equations by the Finite Element Method*. Mineola, NY: Dover Publications.

Kaban, M. K., Petrunin, A. G., Schmeling, H. and Shahraki, M. (2014a). Effect of decoupling of lithospheric plates on the observed geoid. *Surv. Geophys.*, *35*(6), 1361–1373.

Kaban, M. K., Schwintzer, P., Artemieva, I. M. and Mooney, W. D. (2003). Density of the continental roots: compositional and thermal contributions. *Earth Planet. Sci. Lett.*, *209*, 53–69.

Kaban, M. K., Tesauro, M., Mooney, W. D. and Cloetingh, S. A. P. L. (2014b). Density, temperature, and composition of the North American lithosphere—New insights from a joint analysis of seismic, gravity, and mineral physics data: 1. Density structure of the crust and upper mantle. *Geochem. Geophys. Geosyst.*, *15*(12), 4781–4807.

Karato, S. (2003). *The Dynamic Structure of the Deep Earth: An Interdisciplinary Approach.* Princeton, NJ: Princeton University Press.

Karato, S. (2010). Rheology of the deep upper mantle and its implications for the preservation of the continental roots: A review. *Tectonophysics*, *481*, 82–98.

Karato, S. and Wu, P. (1993). Rheology of the upper mantle: A synthesis. *Science*, *260*, 771–778.

Kaufmann, G., Wu, P. and Ivins, E. R. (2005). Lateral viscosity variations beneath Antarctica and their implications on regional rebound motions and seismotectonics. *J. Geodyn.*, *39*(2), 165–181.

King, S. D. (2016). An evolving view of transition zone and midmantle viscosity. *Geochem. Geophys. Geosyst.*, *17*(3), 1234–1237.

Korenaga, J. and Karato, S. (2008). A new analysis of experimental data of olivine rheology. *J. Geophys. Res.*, *113*, B02403.

Kronbichler, M., Heister, T. and Bangerth, W. (2012). High accuracy mantle convection simulation through modern numerical methods. *Geophys. J. Int.*, *191*(1), 12–29.

Landau, L. D. and Lifshitz, E. M. (1987). *Fluid Mechanics* (2 ed.), volume 6 of *Course of Theoretical Physics*. New York: Pergamon Press.

Lowrie, W. (2007). *Fundamentals of Geophysics* (2 ed.). New York: Cambridge University Press.

Marquardt, H. and Miyagi, L. (2015). Slab stagnation in the shallow lower mantle linked to an increase in mantle viscosity. *Nat. Geosci.*, *8*, 311–314.

McKenzie, D. P., Roberts, J. M. and Weiss, N. O. (1974). Convection in the Earth's mantle: Towards a numerical solution. *J. Fluid Mech.*, *62*(3), 465–538.

Melchior, P. J. (1966). *The Earth Tides.* Oxford: Pergamon Press.

Mitrovica, J. X. and Forte, A. M. (2004). A new inference of mantle viscosity based upon joint inversion of convection and glacial isostatic adjustment data. *Earth Planet. Sci. Lett.*, *225*, 177–189.

Morley, L. W. and Larochelle, A. (1964). Paleomagnetism as a means of dating geological events. *Roy. Soc. Canada Spec. Publ.*, *8*, 39–50.

Moucha, R., Forte, A. M., Mitrovica, J. X. and Daradich, A. (2007). Lateral variations in mantle rheology: Implications for convection related surface observables and inferred viscosity models. *Geophys. J. Int.*, *169*(1), 113–135.

Newton, I. (1729). *The Mathematical Principles of Natural Philosophy.* London: Benjamin Motte.

Petrunin, A. G., Kaban, M. K., Rogozhina, I. and Trubitsyn, V. P. (2013). Revising the spectral method as applied to modeling mantle dynamics. *Geochem. Geophys. Geosyst.*, *14*(9), 3691–3702.

Poirier, J.-P. (2000). *Introduction to the Physics of the Earth's Interior* (2 ed.). Cambridge: Cambridge University Press.

Ranalli, G. (2001). Mantle rheology: Radial and lateral viscosity variations inferred from microphysical creep laws. *J. Geodyn.*, *32*, 425–444.

Ritsema, J., Deuss, A., van Heijst, H.-J. and Woodhouse, J. H. (2011). S40RTS: A degree-40 shear-velocity model for the mantle from new Rayleigh wave dispersion, teleseismic traveltime and normal-mode splitting function measurements. *Geophys. J. Int.*, *184*(3), 1223–1236.

Ritsema, J., van Heijst, H.-J. and Woodhouse, J. H. (1999). Complex shear velocity structure imaged beneath Africa and Iceland. *Science*, *286*, 1925–1928.

Rogozhina, I. (2008). *Global modeling of the effect of strong lateral viscosity variations on dynamic geoid and mantle flow velocities.* (Doctoral thesis). Deutsches GeoForschungsZentrum GFZ, Potsdam.

Rowley, D. B., Forte, A. M., Rowan, C. J., Glišović, P., Moucha, R., Grand, S. P. and Simmons, N. A. (2016). Kinematics and dynamics of the East Pacific Rise linked to a stable, deep-mantle upwelling. *Sci. Adv.*, *2*(12), e1601107, doi: 10.1126/sciadv.1601107.

Rudolph, M. L., Lekić, V. and Lithgow-Bertelloni, C. (2015). Viscosity jump in Earth's mid-mantle. *Science*, *350*(6266), 1349–1352.

Schubert, G., Turcotte, D. L. and Olson, P. (2004). *Mantle Convection in the Earth and Planets*. Cambridge University Press.

Sheehan, A. F., Abers, G. A., Jones, C. H. and Lerner-Lam, A. L. (1995). Crustal thickness variations across the Colorado Rocky Mountains from teleseismic receiver functions. *J. Geophys. Res.*, *100*(B10), 20391–20404.

Simmons, N. A., Forte, A. M., Boschi, L. and Grand, S. P. (2010). GyPSuM: A joint tomographic model of mantle density and seismic wave speeds. *J. Geophys. Res.*, *115*(B12), 2156–2202.

Simmons, N. A., Forte, A. M. and Grand, S. P. (2009). Joint seismic, geodynamic and mineral physical constraints on three-dimensional mantle heterogeneity: Implications for the relative importance of thermal versus compositional heterogeneity. *Geophys. J. Int.*, *177*, 1284–1304.

Steinberger, B. and Calderwood, A. R. (2006). Models of large-scale viscous flow in the Earth's mantle with constraints from mineral physics and surface observations. *Geophys. J. Int.*, *167*(3), 1461–1481.

Su, W.-J., Woodward, R. L. and Dziewoński, A. M. (1994). Degree-12 model of shear-velocity heterogeneity in the mantle. *J. Geophys. Res.*, *99*, 6945–6980.

Tozer, D. C. (1965). Heat transfer and convection currents. *Phil. Trans. Roy. Soc. London A*, *258*, 252–271.

Turcotte, D. L. and Oxburgh, E. R. (1967). Finite amplitude convective cells and continental drift. *J. Fluid Mech.*, *28*(1), 29–42.

Van der Wal, W. (2009). *Contributions of Space Gravimetry to Postglacial Rebound Modeling with Different Rheologies*. (Doctoral thesis). University of Calgary.

Van der Wal, W., Whitehouse, P. L. and Schrama, E. J. O. (2015). Effect of GIA models with 3D composite mantle viscosity on GRACE mass balance estimates for Antarctica. *Earth Planet. Sci. Lett.*, *414*, 134–143.

Vine, F. J. and Matthews, D. H. (1963). Magnetic anomalies over oceanic ridges. *Nature*, *199*, 947–849.

Zhang, S. and O'Neill, C. (2016). The early geodynamic evolution of Mars-type planets. *Icarus*, *265*, 187–208.

Zhong, S., Zuber, M. T., Moresi, L. and Gurnis, M. (2000). The role of temperature-dependent viscosity and surface plates in spherical shell models of mantle convection. *J. Geophys. Res.*, *105*, 11063–11082.